

## QFM: quenching flamelet-generated manifold for modelling of flame–wall interactions

Denis V. Efimov, Philip de Goey & Jeroen A. van Oijen

To cite this article: Denis V. Efimov, Philip de Goey & Jeroen A. van Oijen (2019): QFM: quenching flamelet-generated manifold for modelling of flame–wall interactions, *Combustion Theory and Modelling*, DOI: [10.1080/13647830.2019.1658901](https://doi.org/10.1080/13647830.2019.1658901)

To link to this article: <https://doi.org/10.1080/13647830.2019.1658901>



© 2019 The Author(s). Published by Informa UK Limited, trading as Taylor & Francis Group



[View supplementary material](#)



Published online: 29 Aug 2019.



[Submit your article to this journal](#)



Article views: 46



[View related articles](#)



[View Crossmark data](#)



## QFM: quenching flamelet-generated manifold for modelling of flame–wall interactions

Denis V. Efimov \*<sup>1</sup>, Philip de Goeij  and Jeroen A. van Oijen 

*Department of Mechanical Engineering, Eindhoven University of Technology, Eindhoven,  
The Netherlands*

(Received 13 December 2018; accepted 29 July 2019)

This work introduces a new method to improve the accuracy of the flamelet-generated manifold (FGM) method under conditions of flame–wall interactions (FWI). Special attention is given to the prediction of the pollutant CO.

In existing FGM methods, in order to account for heat loss, usually flamelets with constant enthalpy are utilised. These constant enthalpy flamelets used to generate the manifold, do not include the effects of wall heat loss on the manifold composition, resulting in simulation inaccuracies in the near-wall region, where large enthalpy gradients are present. To address this issue, the idea to utilise 1D head on quenching (HOQ) flamelets for tabulated chemistry is adopted and applied here in the context of the FGM method. The HOQ qualitatively resembles the general phenomena of FWI. However, the rates of wall heat loss and the accompanied effects on the chemical species composition may quantitatively differ between various FWI configurations. In addition, the magnitude of heat transfer rate may vary in space and time in general configurations. Therefore, in this work, a method is introduced to generate a 3D manifold, based on multiple HOQ-like flamelets, that includes the variation of the rate of heat loss as an extra table dimension. This dimension is parametrised by a second reaction progress variable for which a transport equation is solved next to the equations for enthalpy and the first progress variable.

The new developed method, referred to as Quenching Flamelet-generated Manifold (QFM), is described in this work. Further, the method is validated against detailed chemistry simulations of a two-dimensional premixed laminar side-wall quenching of a methane-air flame. A comparison is presented, analysing the performance obtained using the existing 2D FGM method, a 2D QFM that is based on a single HOQ flamelet which does not account for a varying rate of wall heat loss and a 3D QFM, which does. Finally, it is shown that the 3D QFM tabulated chemistry simulation yields a very good level of accuracy and that the accuracy for prediction of CO concentrations near the wall is improved tremendously.

**Keywords:** flame modelling; reduced chemistry; flame–wall interaction; side-wall quenching; prediction of emissions; flamelet-generated manifold (FGM); additional chemical time scales

---

\*Corresponding author. Email: [D.V.Efimov@tue.nl](mailto:D.V.Efimov@tue.nl)

### List of abbreviations

DC	detailed chemistry
FGM	flamelet-generated manifold
FWI	flame/wall interactions
HOQ	head on quenching
QFM	quenching flamelet-generated manifold
REDIM	reaction diffusion manifolds
SWQ	side-wall quenching

### List of symbols

$\alpha_{i,j}$	linear coefficient of species $i$ in the definition of progress variable $j$
$\kappa$	curvature
$\lambda$	thermal conductivity
$\xi$	arc-length tangential to the flame surface
$\rho$	density
$\tau$	stress tensor
$\phi_i$	boundary flux of species $i$
$\omega$	chemical source term
$c_p$	specific heat capacity at constant pressure
$h$	enthalpy
$K$	mass-based stretch rate
$m$	mass flux
$m_b$	mass burning rate
$m_{in}$	boundary mass flow rate
$M_i$	molar mass of species $i$
$\mathbf{n}$	vector normal to the flame surface
$N_r$	number of chemically reactive manifold dimensions
$N_s$	number of chemical species
$p$	pressure
$\mathbf{q}$	vector tangent to the flame surface
$Q_{Y_i}$	$Q$ -term of species $i$
$s$	arc length perpendicular to the flame surfaces
$s_L$	laminar burning velocity
$T$	temperature
$t$	time
$\mathbf{u}, [u_x, u_y]$	velocity vector
$x$	spatial coordinate
$y$	spatial coordinate
$\gamma$	reaction progress variable
$Y_i$	mass fraction of species $i$

## 1. Introduction

Flame/wall interaction (FWI) is a broadly studied topic [1] as it is frequently occurring in various types of combustion equipment [2–4]. The effects of FWI entail deteriorating processes such as heat loss, incomplete combustion and formation of pollutants, specifically

CO. The design of numerous combustion applications would hence benefit from simulation tools able to accurately model FWI. Detailed chemical models generally provide a reliable representation of combustion processes. However, these models cannot be employed easily for the simulation of realistic industrial applications, due to their high computational costs and numerical complexity arising in 3D geometries and turbulent flows. Therefore, reduced chemical models are required. In addition, due to current environmental concerns and the development in regulations, the design of combustion equipment is focusing on the reduction of pollutants emissions, such as carbon monoxide and  $\text{NO}_x$  while maintaining high efficiency. Consequently, a reduced chemical model would be very welcome to be able to give accurate predictions of pollutants formation in the presence of FWI.

The general phenomenon of FWI can be subdivided into distinct types according to the physical flow conditions [1]. Head on quenching (HOQ) occurs when a flame propagates towards the wall under a perpendicular angle. At a certain small distance the flame starts to loose heat to the wall and eventually quenches. Several studies of HOQ configuration have been performed, e.g. [5,6]. Commonly, laminar HOQ configuration is modelled by means of a one-dimensional transient simulation. Another important type of FWI is side-wall quenching (SWQ) [7,8], described by a flame front propagating parallel to a cold wall. In that case, quenching occurs only in the near-wall part of the flame. A recently proposed stationary FWI configuration shows advantages in various aspects in understanding FWI [9]. In this type of FWI, the heat loss is directed from the flame zone to the burnt mixture, unlike the situation in the HOQ and SWQ configurations.

In the recent literature, several authors have focused on the numerical modelling of carbon monoxide CO in flames involving FWI. The work of Ganter *et al.* [10] investigated the phenomenology of CO formation under conditions of SWQ. Various detailed and reduced chemical models were validated against experimental measurements. The detailed chemistry results for CO were shown to be in a good agreement with the experimental data. Therefore, also in this study the detailed chemistry simulation is used as reference for the validation of the reduced models. On the other hand, in [10], the CO predictions obtained with the flamelet-generated manifold (FGM) reduced chemistry model showed deviations in the near-wall region. A Lagrangian analysis of CO transport and chemistry was applied, showing that higher CO concentrations near the wall are mainly associated with the diffusive transport towards the wall. That explained the errors found by FGM, as the manifold was generated utilising 1D flat flames with constant enthalpy where this effect is not included. Steinhilber *et al.* [11] and Ganter *et al.* [12] applied reaction diffusion manifolds (REDIM) to model respectively HOQ and SWQ configurations. The gradient of enthalpy in the near-wall region, and the associated transport of species were indicated as crucial physical processes and taken into account during the generation of the manifolds. The scalar gradients, required for the REDIM solution, were estimated from a one-dimensional HOQ simulation, which resulted in a better resemblance of the underlying physics.

The objective of this work is to develop an improved flamelet-generated manifold (FGM) [13–15] chemistry reduction method, providing an accurate representation of thermochemistry in the presence of FWI, focusing on the prediction of emissions. Following the idea of [12], the one-dimensional HOQ configuration is utilised as a representative flamelet type to generate a manifold in composition space. In counterpart to steady burner-stabilised flamelets, HOQ qualitatively resembles more complex configurations involving FWI and includes the diffusive transport of CO towards the wall, as identified in [12]. However, quantitatively the rate of heat loss and the accompanied

**scalar dissipation** of species may differ between FWI configurations or exhibit time-dependent variation in transient and turbulent flows [16,17]. To improve the accuracy, this variation of the rate of cooling is included in the manifold as an extra parameter. Previously FGM has been extended with additional chemically reactive dimensions to account for the effects of fast cooling and expansion on the post-flame pollutants chemistry [18]. In this work, one additional manifold dimension, parametrised by a secondary progress variable, will be introduced to account for the variations of the rate of wall heat loss coupled with their impact on thermochemistry. The primary focus lies in achieving accurate FGM predictions for CO formation in the near-wall region, while retaining the simplicity of application and the high performance of the method. The scope of the method also includes improving FGM accuracy for more general parameters, such as flame shape, heat loss to the wall and the remaining thermochemical composition.

Similarly to the literature, an idealised SWQ test configuration is utilised in this work. The performance of several FGM models is validated against the detailed chemistry simulation, showing that the highest accuracy is obtained when the FGM is not only based on an HOQ flamelet but is also extended with an extra degree of freedom accounting for the magnitude of the rate of heat loss.

In Section 2, the test simulation setup is described along with the detailed chemistry (DC) simulation results. Section 3 presents the predictions from the FGM generated from a series of adiabatic flamelets, obtained by varying the values of the inlet enthalpy per flamelet. In this way, the heat loss is included in the 2D manifold in composition space utilising enthalpy as an extra parameter next to the reaction progress variable. This method, introduced in van Oijen and de Goey [13], is further referred in this work as the ‘standard FGM’. The configuration and the practical application of the standard FGM are outlined, comprising the fundamental basis to be extended by the new introduced methods. Section 3 shows that the CO chemistry in the near-wall region indeed cannot be treated accurately by the standard FGM. Additionally, this section demonstrates the predictive capability of solving a transport equation for CO mass fraction in the context of standard FGM. The improvements that are found by transporting CO are discussed along with the reasons for the remaining inaccuracies. Section 4 contains an analysis demonstrating the differences in CO phenomenology between standard FGM and detailed chemistry, providing a physical motivation for the novel method introduced further in this work. In Section 5, the FGM method is extended for FWI pollutants modelling by generating a higher dimensional manifold composed of a series of HOQ flamelets with varying cooling rate. This method is referred to as the quenching flamelet-generated manifold ‘QFM’. The simplest configuration of QFM involves tabulating a single HOQ flamelet as function of two control variables, enthalpy and progress variable, resulting in a 2D manifold in composition space. This 2D QFM does not include the effect of the variation of the rate of cooling, assuming it to take a fixed value. Utilising a series of HOQ flamelets computed varying the cooling rate, the thermochemistry is tabulated as the function of three control variables, resulting in a manifold in composition space denoted as the 3D QFM. The results obtained with the new introduced technique are validated and compared to the standard FGM, showing that the new method yields accurate results for the flame shape and thermochemical composition, and in particular for CO. Finally, conclusions and recommendations are given in Section 6.

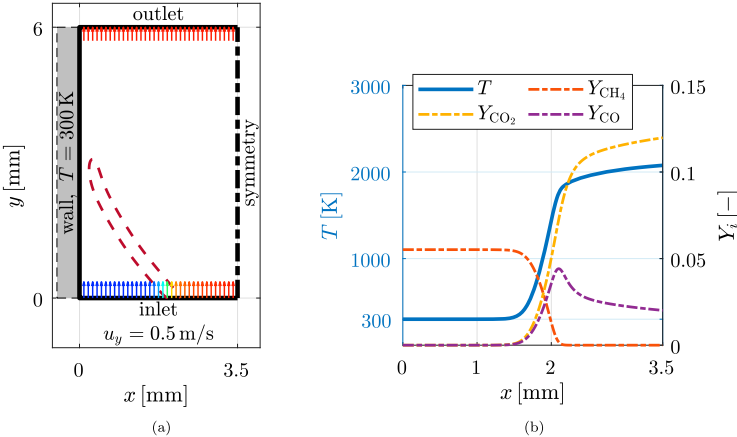


Figure 1. Left: A schematic drawing of the geometry of the test case, including a contour of the rate of heat release corresponding to 10 % of its maximum value. Right: A plot of the inlet boundary conditions at  $y = 0$  mm as the function of  $x$ . (a) A sketch of the computational domain, the colour of the arrows indicates the temperature: blue – unburnt, red – burnt. (b) The profiles for temperature and species mass fractions at the inlet boundary.

## 2. Detailed chemistry SWQ analysis

### 2.1. SWQ configuration

In this work, a simulation of the SWQ configuration is considered as a test setup. A schematic of the simulation geometry is depicted in Figure 1(a). A premixed flame is stabilised in a rectangular domain of  $L_x \times L_y$  given by  $3.5 \times 6$  mm. An isothermal wall ( $T_{\text{wall}} = 300$  K) is placed at the left boundary of the domain at  $x = 0$  mm. At the inlet, located at  $y = 0$  mm, a gas mixture composition profile of a one-dimensional adiabatic freely propagating premixed flame is imposed as the function of the  $x$ -coordinate along the boundary. This one-dimensional flame is corresponding to the stoichiometric methane–air mixture at atmospheric pressure and unburnt temperature given by  $T_u = T_{\text{wall}} = 300$  K, resulting in a burning velocity of  $s_L = 29.6$  cm/s. The applied inlet profiles for temperature and several chemical species are shown in Figure 1(b). A constant  $y$ -velocity of 0.5 m/s and  $x$ -velocity equal to zero are prescribed at the inlet boundary.

### 2.2. Numerical setup

The simulations are performed in a geometry with two spatial dimensions and using a steady-state assumption, which allows to maintain sufficiently low computational costs for detailed chemical model to be applied. The utilised detailed reaction kinetics scheme is DRM19 [19] comprised of  $N_s = 21$  chemical species and 84 reactions. In addition, a unity Lewis numbers diffusion model is adopted, following the work of Ganter *et al.* [10], where it was found to be sufficiently accurate for analogous conditions. In the general context of FGM reduced chemistry, preferential diffusion can be accounted for following the previously developed methods [20,21]. All simulations are performed using a finite volume solver<sup>1</sup> with a second-order upwind discretisation scheme. A constant mesh size of  $6.25 \mu\text{m}$  is used, resulting in total of roughly  $0.5 \cdot 10^6$  cells. A symmetry boundary condition is imposed at the right boundary of the domain,  $x = 3.5$  mm and a no-slip isothermal condition is applied at the wall boundary. Along with the two-dimensional Navier–Stokes

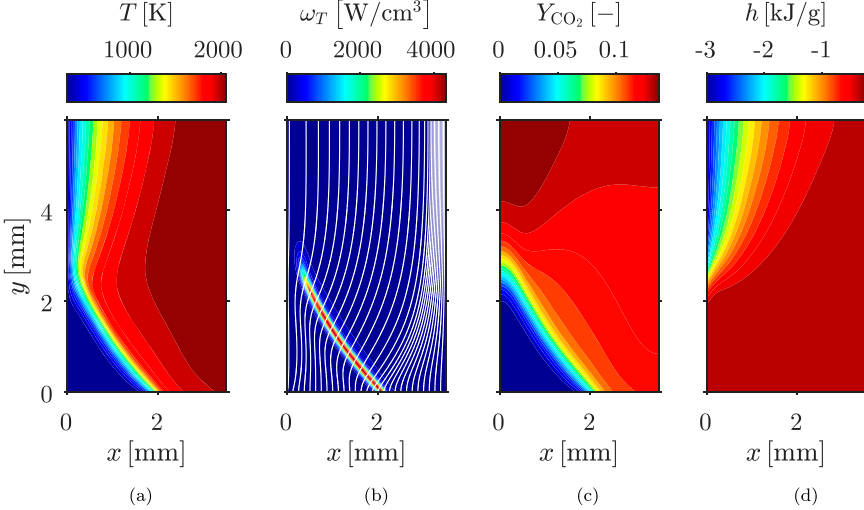


Figure 2. A global illustration of the simulation results. From left to right: temperature (a), volumetric rate of heat release,  $\omega_T$  (b), including streamlines (in white) indicating the direction of the velocity, the mass fraction of  $\text{CO}_2$  (c) and specific enthalpy,  $h$  (d).

equations, the transport equations for species mass fractions and enthalpy are solved. Under steady-state and unity Lewis numbers assumptions, these equations are given by

$$\nabla \cdot (\rho \mathbf{u}) = 0, \quad (1a)$$

$$\nabla \cdot (\rho \mathbf{u} \mathbf{u}) = -\nabla p - \nabla \cdot \boldsymbol{\tau}, \quad (1b)$$

$$\nabla \cdot (\rho \mathbf{u} Y_i) - \nabla \cdot \left( \frac{\lambda}{c_p} \nabla Y_i \right) = \omega_i, \quad i = 1, \dots, N_s - 1, \quad (1c)$$

$$\nabla \cdot (\rho \mathbf{u} h) - \nabla \cdot \left( \frac{\lambda}{c_p} \nabla h \right) = 0, \quad (1d)$$

where  $\boldsymbol{\tau}$  is the stress tensor. Note that the energy is solved in the form of the sum of sensible and chemical enthalpy  $h$ , Equation (1d), which is conserved by chemical reactions under the constant pressure approximation. Viscous heating and radiation are not taken into account in Equation (1d).

### 2.3. Results and discussion

This section presents the results of the simulation of the SWQ flame described in Section 2.1. Figure 2 globally illustrates the obtained flame shape. The depicted variables are temperature,  $T$ , volumetric rate of chemical heat release,  $\omega_T$ , the mass fraction of  $\text{CO}_2$  and specific enthalpy,  $h$ . It can be observed that the premixed flame, applied at the inlet, is propagating towards the wall as the height,  $y$ , increases. The flame front is located at  $x \approx 2$  mm of the inlet plane. It propagates under an angle of about  $50^\circ$  and reaches the wall at  $y = 2.5$  mm. From that point on, the mass fraction of  $\text{CO}_2$  near the wall is increasing over the  $y$ -coordinate (Figure 2c) as the mixture composition is evolving towards a burnt state. Consequently, the flame starts to loose heat to the isothermal wall, resulting in an increasing deficit of enthalpy that propagates from the wall into the domain (Figure 2d).

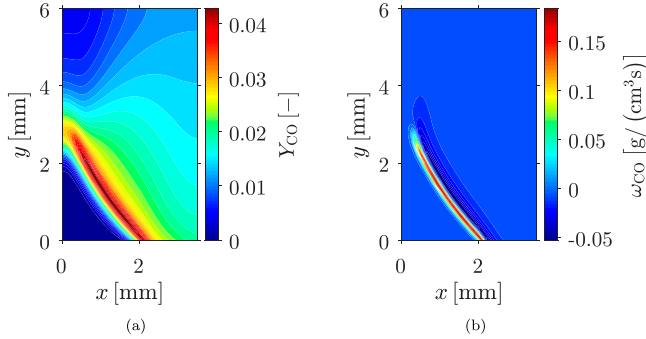


Figure 3. Contours of the mass fraction of CO (a) and its chemical source term,  $\omega_{CO}$  (b).

Figure 3 shows the mass fraction of CO and its chemical source term. Considering the source term, it can be seen that its magnitude in the near-wall region becomes negligible compared to the values in the near adiabatic region. In the near-wall region,  $Y_{CO}$  attains peak values that are 30 % lower than in the unperturbed flame. This presence of CO in the near-wall region without chemical source term is a consequence of diffusive transport, which was already shown in [10].

### 3. Standard FGM applied to SWQ

This section presents the results obtained applying the standard FGM method to simulate the SWQ test case described in Section 2. The methods used to generate the FGM and to apply it in the simulation are described in Section 3.1. The obtained results are presented and compared to those of the DC simulation in Section 3.3.

#### 3.1. Standard FGM numerical setup

The FGM is generated from adiabatic, isobaric premixed stoichiometric methane–air flamelets. A free premixed flamelet configuration is utilised for the maximum enthalpy level, corresponding to an unburnt mixture temperature of  $T_u = 300$  K. The remaining flamelets at lower enthalpy levels are computed using a burner-stabilised configuration [14], with the temperature of the burner set equal to the wall temperature,  $T_{wall} = 300$  K. A series of these flamelets is computed, prescribing inlet mass flux as a parameter that is lowered in steps in order to achieve higher magnitudes of heat loss to the burner. The standard FGM is parametrised by two control variables, enthalpy  $h$  and the reaction progress variable  $\mathcal{Y}$ . Following [15], the progress variable is defined as the sum of the specific mole numbers,  $Y_i/M_i[\text{mol}_i/\text{g}_{\text{mix}}]$  of species H<sub>2</sub>, H<sub>2</sub>O and CO<sub>2</sub>, where  $M_i$  is the molar mass of species  $i$ . For visualisation purposes, the progress variable is multiplied by a factor of 100 to make its maximum value in the order of unity. The flamelets are then stored in a two-dimensional table on a  $609 \times 472$  ( $h \times \mathcal{Y}$ ) curvilinear grid. Figure 4 displays the chemical source term of the reaction progress variable in the manifold and illustrates the tabulation grid. The enthalpy table grid is equidistant, while the grid of the progress variable table dimension is non-equidistant and identical to the grid distribution in the adiabatic freely propagating premixed flamelet with  $T_u = 300$  K. Note that

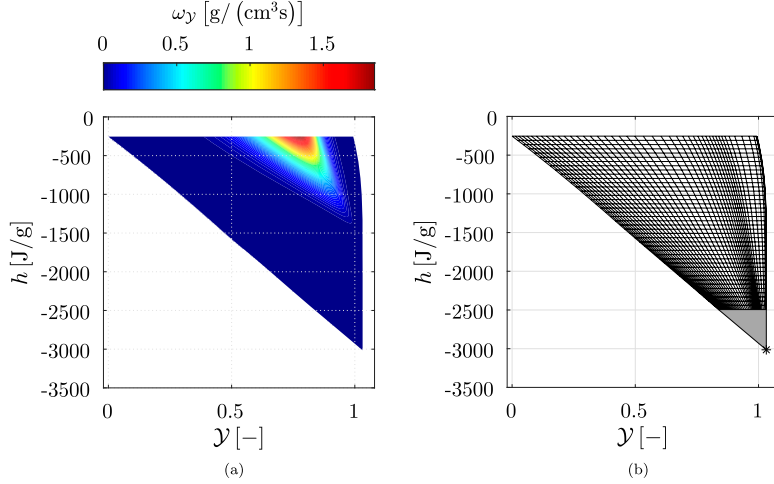


Figure 4. Illustration of the standard FGM: source term of the progress variable and the tabulation mesh. (a) Contour plot of the chemical source term of the reaction progress variable  $\omega_Y$  shown in the space of the FGM control variables. (b) A schematic plot of the curvilinear tabulation grid. The data for species composition in the grey-shaded part of the manifold is obtained by linear interpolation to the chemical equilibrium point at  $T = 300$  K, which is indicated by an asterisk.

there is no flamelet data available below the enthalpy level of  $h \approx -2500$  J/g, as indicated in the plot. This is caused by the flame temperatures being below the flammability limits, resulting in extinction. Manifold data in this region is reconstructed following the method in [13]. The species composition in that remaining part of the manifold is obtained by linear interpolation between the flamelet with the lowest enthalpy and the chemical equilibrium point at  $T = 300$  K. The dependent thermochemical variables, such as temperature, density and chemical source terms are then computed in this part of the manifold as the function of the enthalpy, pressure and species composition. The FGM simulations, including the ones appearing in the later sections, are performed using the same numerical settings as the DC simulation described in Section 2.2. The only difference lies in  $N_s - 1$  species equations being replaced by only a few transport equations for control variables. The transport equation for enthalpy,  $h$ , is solved as a control variable during the FGM simulation. Its form is similar to the one included during the detailed simulation, and it is given by Equation (1d). The transport equation for the reaction progress variable  $\mathcal{Y}$  can be derived by taking a linear combination of the transport equations of species and it is given by

$$\nabla \cdot (\rho \mathbf{u} \mathcal{Y}) - \nabla \cdot \left( \frac{\lambda}{c_p} \nabla \mathcal{Y} \right) = \omega_Y. \quad (2)$$

In addition to the control variables equations, the two-dimensional Navier–Stokes equations, Equations (1a) and (1b), are solved. During runtime, all required transport coefficients, density and the source term of progress variable are looked up in the manifold by means of linear interpolation.

### 3.2. Modelling of CO with FGM

In the context of tabulated chemistry, the mass fraction of any chemical species, including that of CO can be looked up directly from the manifold as the function of the control variables during postprocessing. In an attempt to increase the FGM accuracy for CO predictions, an additional transport equation for its mass fraction is solved in the FGM simulation. This is analogous to the methods for solving a transport equation for  $\text{NO}_x$  [22–24]. This allows the FGM prediction for the mass fraction of CO to attain values not residing in the manifold for given values of the control variables. In this way, the CO concentration can evolve according to its own time scale, accounting for possible perturbations from the manifold due to the effect of transport terms. This transport balance is given in Equation (1c), while a special treatment is adopted for its chemical source term  $\omega_{\text{CO}}$ . Namely, the value of  $\omega_{\text{CO}}$  looked up from the manifold is scaled linearly in order to account for a changed transported CO mass fraction  $Y_{\text{CO}}^{\text{tr}}$  as compared to its local value at the manifold  $Y_{\text{CO}}^{\text{FGM}}$ . The total source term  $\omega_{\text{CO}}$  is split into two parts representing the sum of the contributions of reactions forming CO,  $\omega_{\text{CO}}^+$ , and the sum of the ones consuming it,  $\omega_{\text{CO}}^-$ . Then  $\omega_{\text{CO}}^-$  is linearised in CO mass fraction, resulting in a total source term that includes a two-way coupling with the equation and reads

$$\omega_{\text{CO}} = \omega_{\text{CO}}^+ + Y_{\text{CO}}^{\text{tr}} \left( \frac{\omega_{\text{CO}}^-}{Y_{\text{CO}}^{\text{FGM}}} \right). \quad (3)$$

In the above equation, the terms  $\omega_{\text{CO}}^+$  and  $(\omega_{\text{CO}}^- / Y_{\text{CO}}^{\text{FGM}})$  are stored in the table. Feedback on other species and source terms, such as in FGM-REDx [18], is not included utilising this method. The predictions obtained by this method will be compared to those found by looking up the CO mass fraction directly from the manifold.

### 3.3. Results with standard FGM

#### 3.3.1. Control variables

In Figure 5, standard FGM simulation results are shown for the FGM control variables  $\mathcal{Y}$  and  $h$ . The graph at the left depicts the contours of the reaction progress variable  $\mathcal{Y}$ , while the plot at the right shows the contours of enthalpy  $h$ . It can be observed, looking at the region where the flame touches the wall, that at the upstream locations the standard FGM yields a correct prediction of the progress variable. Further downstream the FGM results have a tendency to underpredict the increase of the progress variable, eventually resulting in an incorrectly estimated shape of the progress variable in the upper half of the domain. At first glance, the global shape of the FGM results for enthalpy appear to correspond well to the detailed chemistry predictions. The underprediction of the progress variable can be observed in more detail from the profiles plotted over the wall (at  $x = 0 \text{ mm}$ ) and two wall-normal lines at  $y = 2.5 \text{ mm}$  and  $2.85 \text{ mm}$  shown in Figure 6. The two chosen wall-normal locations are representing the states of the reaction progress at the wall being respectively 50 % and 75 % of its maximum value. The corresponding locations of these three lines are indicated in white in Figure 5(a). As can be observed, the results of standard FGM, shown in red, are agreeing with DC results in the upstream region, while the underprediction becomes gradually larger with increasing height  $y$ . The underpredicted values for  $\mathcal{Y}$  translate to an underpredicted rate of decrease of enthalpy, as observed in the  $h$  plots in the same figure. In addition to that, the location of the peak value of the progress variable source term,  $\omega_{\mathcal{Y}}$ , is predicted to move too slow towards the wall with increasing  $y$ .

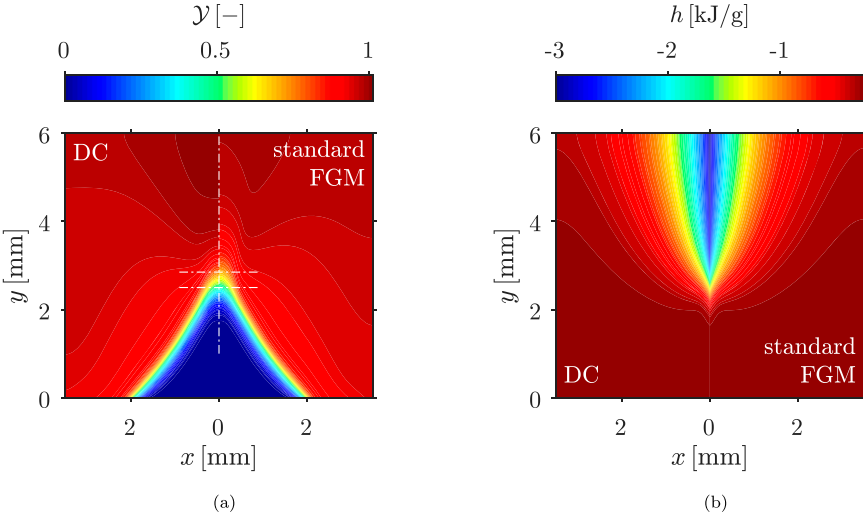


Figure 5. Standard FGM simulation results (right panel) for the two control variables, progress variable  $\mathcal{Y}$  (a) and enthalpy  $h$  (b). The detailed chemistry (DC) results are shown for the reference at the left of each panel. Dashed lines in plot (a) indicate the three locations ( $x = 0, y = 2.5; 2.85$  mm) used later in this work to display 1D profiles of thermochemical variables.

Also, note the difference in scales of  $\omega_{\mathcal{Y}}$  values between the three locations. At the wall, the DC predictions for the progress variable source term are very small, being 2 orders of magnitude lower than its maximum value. There the FGM prediction yields a dissimilar order of magnitude. This, however, does not have a large influence on the solution due to insignificant magnitude of the source term at the wall.

### 3.3.2. CO mass fraction

In Figure 7, a comparison is presented for the CO mass fraction displayed as the function of the control variables. The detailed chemistry results in the control variables space composition are shown in subplot (c), while those corresponding to the direct lookup in the standard FGM are given in subplot (a). The obtained results are comparable to those reported for an analogous case by Ganter *et al.* [10]. Namely, the DC predictions show high CO concentrations also at the low enthalpy levels. This is explained by a strong effect of CO diffusion in the direction of decreasing enthalpy from the adiabatic region, where its main formation is taking place. Looking at the values in the manifold, Figure 7(a), it can be observed that this effect is not present in the FGM generated from constant-enthalpy flamelets, as in that case diffusion only occurs along the constant-enthalpy lines. Figure 8 shows the standard FGM results for the mass fraction of CO in physical space, found utilising two methods: the graph at the left (a) represents the results obtained by direct lookup and subplot (b) shows the values found by solving a transport equation for CO mass fraction accounting for a two-way coupling of the chemical source term,  $\omega_{\text{CO}}$ . As can be observed, the  $Y_{\text{CO}}^{\text{FGM}}$  obtained by direct lookup yields incorrect results in the non-adiabatic region that is located close to the wall in the downstream part of the domain. There the direct lookup predicts a negligibly low concentration, which is in agreement with the absence of CO below  $h = -1500$  J/g shown in Figure 7(a) in the space of the control variables. A moderate improvement of the CO prediction is obtained by solving the transport equation (Figure 8b). Near the wall,

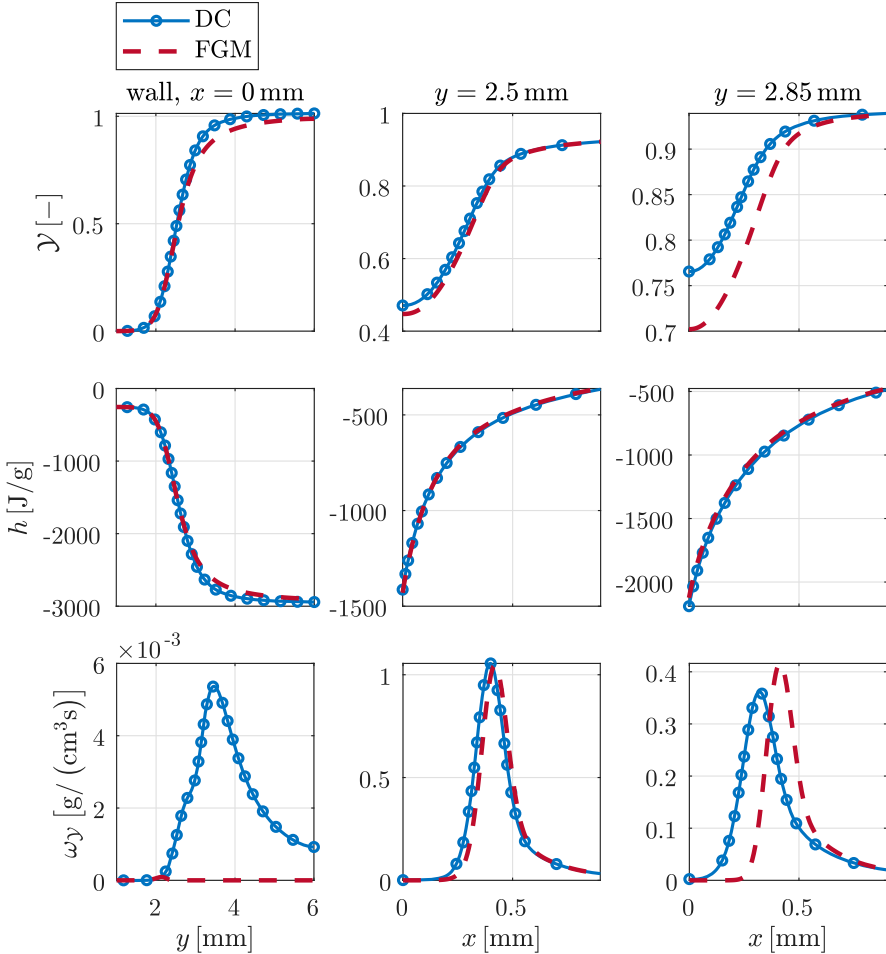


Figure 6. Profiles of various variables: progress variable  $\mathcal{Y}$ , enthalpy  $h$  and the source term of progress variable  $\omega_{\mathcal{Y}}$ , displayed at the left as the function of  $y$  over the wall ( $x = 0$  mm), in the middle and at the right as the function of  $x$  at respectively  $y = 2.5$  mm and  $2.85$  mm.

upstream from the peak CO location, the transported CO contours are matching those of the detailed chemistry. However, CO is overpredicted in the downstream part of the non-adiabatic region yielding an incorrect shape, which can be, among other reasons, attributed to the underestimation of progress variable and the rate of heat loss in that region. The transported  $Y_{CO}$  results are shown as the function of the local values of the FGM control variables in Figure 7(b). As can be seen, high CO concentrations are found in the region where enthalpy is below  $-1500$  J/g, showing that this reduced model for CO is in a much better agreement with DC than the direct lookup. Evidently, diffusion of CO in the direction of enthalpy is in a good qualitative agreement with the results of the detailed model, when displayed in composition space. A correct CO prediction in terms of the FGM control variables indicates that an accurate solution for control variables would have produced a good agreement for transported CO, also in physical space. This observation may suggest that the discrepancies between the transported CO and DC values in physical space

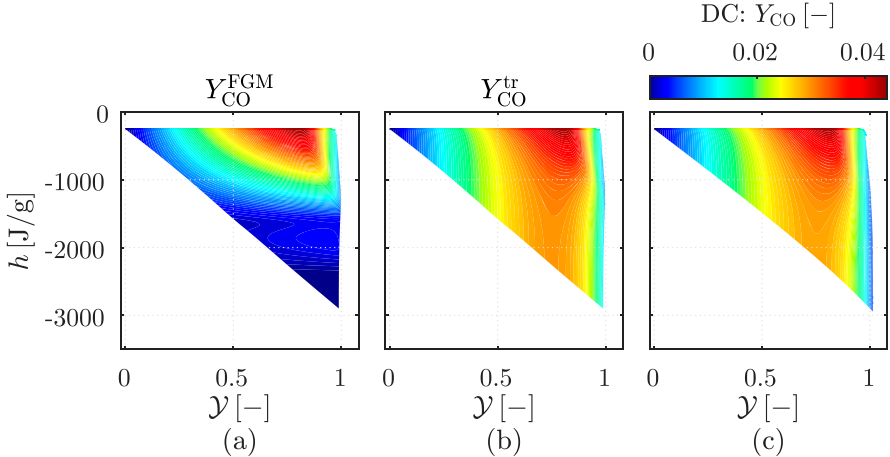


Figure 7. Mass fraction of CO in the space of FGM control variables,  $\mathcal{Y}$  and  $h$ . (a) Value obtained by direct lookup in the manifold  $Y_{\text{CO}}^{\text{FGM}}$ . (b) Standard FGM simulation results for CO obtained by solving an additional transport equation for  $Y_{\text{CO}}^{\text{tr}}$ . (c) Detailed chemistry results for CO.

(Figure 8b) are mainly caused by the inaccurate predictions of the profiles of the control variables, especially progress variable  $\mathcal{Y}$ , in the standard FGM simulation.

The profiles for CO mass fraction and its chemical source term over the wall at  $x = 0$  mm and wall-normal lines at  $y = 2.5$  mm and  $y = 2.85$  mm are given in Figure 9. The results obtained by direct lookup from the manifold as function of the local values of the control variables are showing a different trend, compared to the DC predictions. The direct lookup generally predicts incorrectly low CO values in the near-wall region. On the other hand, transported CO results are benefiting from taking diffusion fluxes towards the wall into account. Over the wall, correct predictions are obtained up to the peak CO location, while further downstream it yields an overestimation by a factor 2. The magnitude of the source term at the wall, for both DC and FGM, is negligibly small compared to its maximum value, and its underprediction by the FGM probably has only an insignificant influence on the solution. The horizontal profiles show that transported CO is in a good agreement with detailed chemistry at the upstream location of  $y = 2.5$  mm, while its source term prediction is shifted away from the wall and attains a higher magnitude as compared to the DC profiles. At the downstream horizontal location of  $y = 2.85$  mm, due to an increasing underprediction of the progress variable, the source term of CO obtained with the standard FGM shows an even higher discrepancy compared to DC. This translates in the overestimation of the transported CO observed there. In its turn, the prediction of the chemical source term strongly depends on the accuracy of the control variables.

It can be concluded that solving a transport equation for CO, results in a better agreement with the DC, while the adoption of the linear correction of the chemical source term of CO improves the  $\omega_{\text{CO}}$  accuracy to some minor degree. It is also worth mentioning, that another method for modelling of  $\omega_{\text{CO}}$  has been considered, namely the transport equation was solved looking up the source term directly in the manifold without linearisation. As a result, which is omitted here for brevity, unrealistic predictions of CO mass fraction were obtained in the post-flame zone. This is explained by an absence of the feedback of the transported CO mass fraction on its chemical source term, resulting in  $Y_{\text{CO}}$  becoming

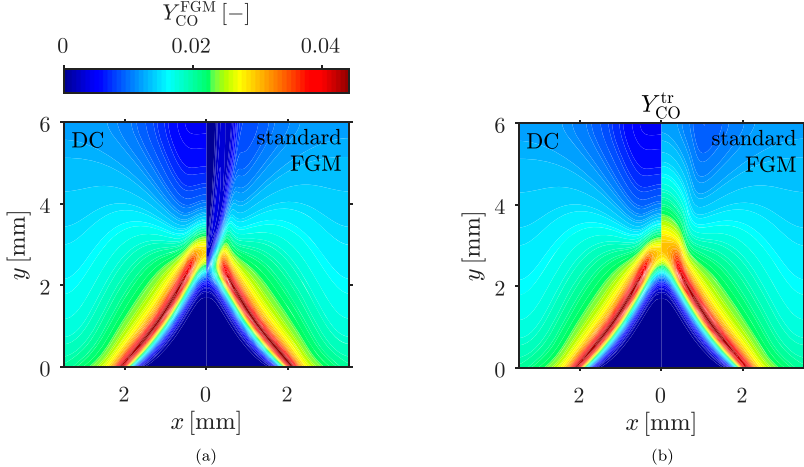


Figure 8. Standard FGM simulations results for the mass fraction of CO found by direct lookup (a) ( $Y_{\text{CO}}^{\text{FGM}}$ ) and a transport equation including a two-way coupling for the source term (b) ( $Y_{\text{CO}}^{\text{tr}}$ ). DC results are shown at the left of each plot for the reference.

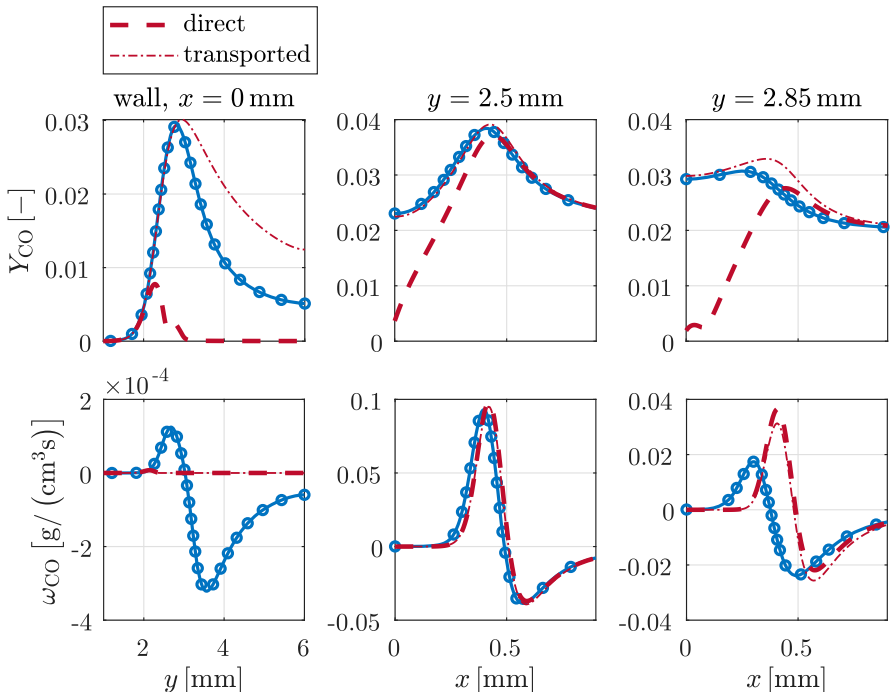


Figure 9. Profiles of mass fraction  $Y_{\text{CO}}$  and source term of CO,  $\omega_{\text{CO}}$ , plotted as the function of  $y$  over the wall ( $x = 0 \text{ mm}$ ) and as the function of  $x$  over the wall-normal lines at  $y = 2.5 \text{ mm}$  and  $y = 2.85 \text{ mm}$ . The FGM CO modelling methods are shown by different line styles with similar colour as indicated in the legend. The legend for the chemistry models (DC and FGM) is similar to that of Figure 6.

unbounded. Nevertheless, the perturbation from the manifold attained by the transported CO evidently exceeds the range where the source term can be assumed to change linearly with the perturbation. Consequently, a more accurate modelling of the involved combustion physics is required to improve the general accuracy for the entire thermochemical composition. This is the topic discussed in the following sections.

#### 4. CO formation analysis in the flame-adapted coordinate system

In order to understand the processes governing the evolution of CO in the quenching region and the origin of the inaccuracies from the standard FGM as observed in Section 3, a coordinate transformation is applied to the detailed chemistry solution for CO, rewriting its transport equation in the flame-adapted coordinate system [25]. As a result, this assessment shows how the FGM method can be further developed to improve the accuracy under conditions of FWI.

Utilising the reaction progress variable,  $\mathcal{Y}$ , the flame adaptive coordinate system in two spatial dimensions is spanned by an orthonormal basis  $\{\mathbf{n}, \mathbf{q}\}$ . The flame surface is referred to as an isosurface of  $\mathcal{Y}$ . The flame-normal vector  $\mathbf{n}$  is locally describing the direction of the flamelet path, orthogonal to the flame surface:

$$\mathbf{n} := \frac{\nabla \mathcal{Y}}{\|\nabla \mathcal{Y}\|}, \quad (4)$$

here it is chosen to point in the direction of the burnt gas mixture. The vector  $\mathbf{q}$  represents the direction tangent to the flame surface and its first and second components can be found from the components of vector  $\mathbf{n}$  by

$$\mathbf{q} = [q_1, q_2] = [n_2, -n_1], \quad (5)$$

ensuring that both vectors have unit length and are orthogonal to each other. The species transport equation (1c) can be written in a quasi-1D form [25]. Under steady-state conditions, it reads

$$\frac{\partial \rho Y_i}{\partial t} = \underbrace{-\frac{\partial m Y_i}{\partial s} + \kappa (m Y_i)}_{\text{Convection}} + \underbrace{\frac{\partial}{\partial s} \left( \frac{\lambda}{c_p} \frac{\partial Y_i}{\partial s} \right) - \kappa \left( \frac{\lambda}{c_p} \frac{\partial Y_i}{\partial s} \right)}_{\text{Diffusion}} + \omega_i - \rho K Y_i + Q_{Y_i} = 0 \quad (6a)$$

with  $t$  being time,  $s$  the arc-length perpendicular to the flame surfaces. Furthermore, the flame curvature  $\kappa$ , the mass flux normal to the flame surfaces  $m$  and the mass-based stretch rate  $K$  [25], are given by

$$\kappa = \nabla \cdot \mathbf{n}, \quad m = \rho \mathbf{u} \cdot \mathbf{n}, \quad \rho K = -\nabla \cdot (m \mathbf{n}), \quad (6b)$$

and the so-called  $Q$ -term of species  $i$ ,  $Q_{Y_i}$ , describing the diffusive transport tangential to the flame surface is computed according to

$$Q_{Y_i} = \frac{\partial}{\partial \xi} \left( \frac{\lambda}{c_p} \frac{\partial Y_i}{\partial \xi} \right) \quad (6c)$$

denoting the arc length in the direction of  $\mathbf{q}$  (tangential to the flame surface) as  $\xi$ . The terms of Equation (6a) indicated as ‘Convection’ and ‘Diffusion’ represent the transport of the

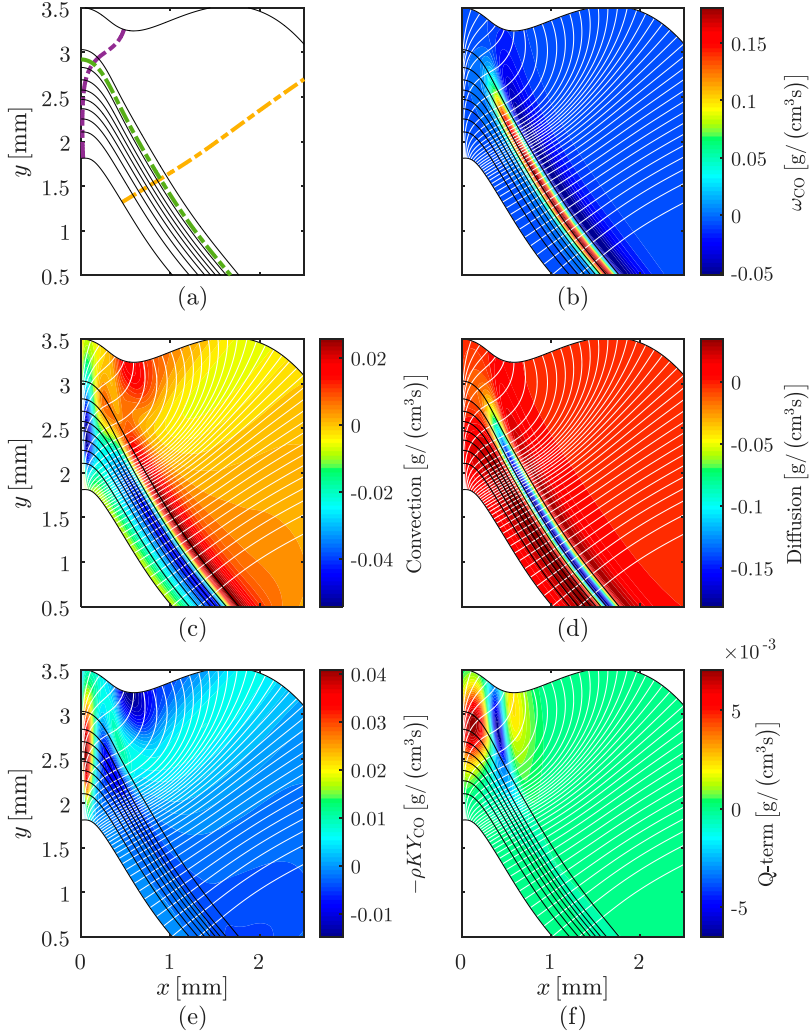


Figure 10. Terms of the CO equation transformed to the flame-adapted coordinate system. In plot (a), the locations of three lines are indicated that are used further to display 1D profiles of the equation terms. In plot (b) the source term of CO is shown, the remaining transport terms are: flame-normal convection (c) and diffusion (d), tangential convective term (e) and Q-term (f).

corresponding type occurring in the flame-normal direction. The stretch rate  $K$  is defined as the fractional rate of change of the mass contained in an infinitesimal control volume moving with the flame.

Figure 10 depicts the values of the contributions of the terms in the CO transport equation in the flame-adapted coordinate system. The paths normal to the flame surface are shown in white while the isolines of progress variable are drawn in black. Plot 10(a) shows the isolines of the progress variable along with the three paths that are used later in this section to present the 1D profiles of various equation terms. The terms are displayed within the area where  $\|\nabla \mathcal{Y}\| \neq 0$ , as the flame-adapted coordinate system is not defined in the unburnt and the post-flame zones, which are left out in white in the figures. Plot (b)

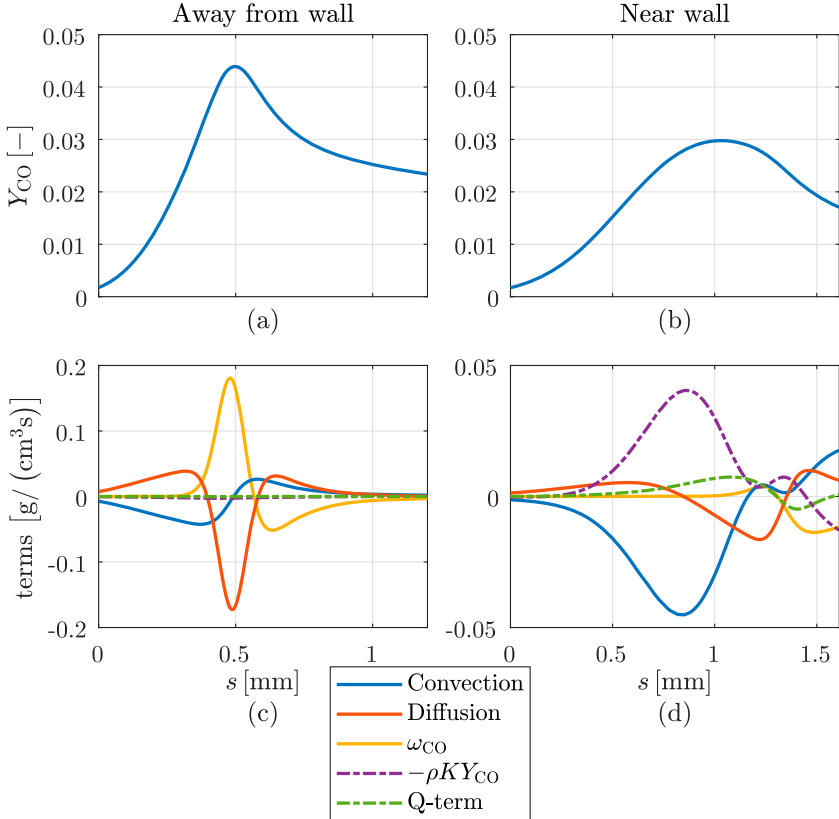


Figure 11. Profiles of the CO mass fraction and the transport terms after coordinate transformation, plotted over flamelet paths normal to the flame surface as the function of arc length  $s$ . (a) and (c) show the flamelet path away from the wall indicated in yellow in Figure 10(a), while (b) and (d) show the path close to the wall drawn in purple in Figure 10(a).

shows the reaction source term of CO. The remaining subplots represent transport in both the direction normal to the flame surface (convection (c), diffusion (d)) and the direction tangent to the flame surface (stretch term,  $-\rho K Y_{CO}$  (e), and  $Q$ -term (f)). Combined, the convection and the stretch term (c + e) represent the effect of total convective transport, while diffusion and the  $Q$ -term added together (d + f) would entail the effect of diffusive transport. Note that positive values of the depicted transport terms correspond to an increase of CO concentration, as stated in Equation (6a). In the region away from the wall, typical adiabatic premixed flamelet conditions are observed in Figure 10. The preheat zone, located upstream from the flame, is characterised by a balance between a slightly negative contribution from the convection term and a positive values of the diffusion, as can be seen from Figures 10(c) and (d). The source term is zero in this area. Further downstream, in the reaction zone a peak of the CO source term is found, accompanied by a large influence of the diffusive transport. Finally, in the post-flame zone, CO is consumed showing a negative chemical source term, while convection and diffusion contributions are both positive representing physical transport of CO from the reaction zone to the post-flame zone. It is worth noting that in this adiabatic area,  $x > 0.5$  mm, the contours of all equation terms are parallel to the isolines of the progress variable and the two tangential transport terms have

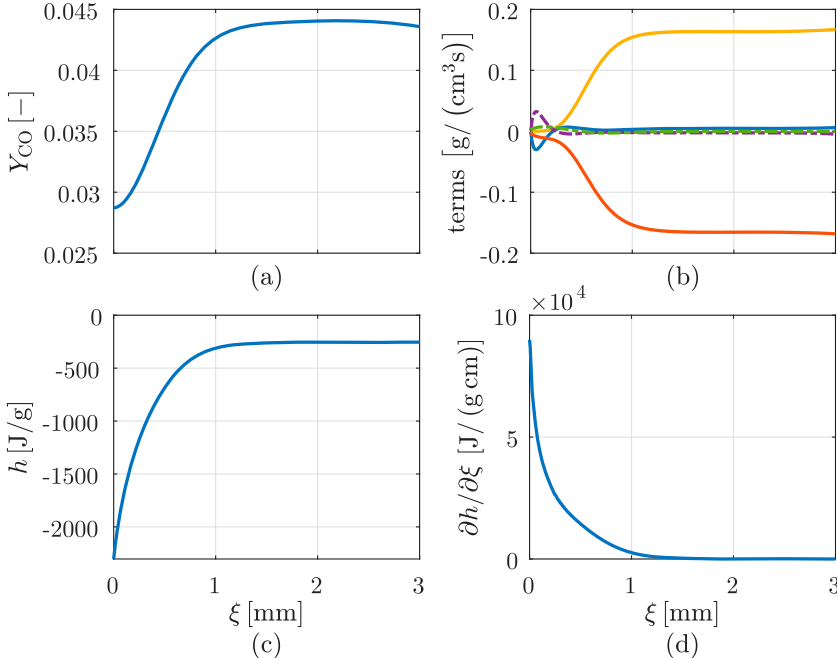


Figure 12. Profiles of the mass fraction of CO, the contributions of various terms in the transport equation, enthalpy and enthalpy gradient plotted over a flame isocontour with  $\mathcal{Y} = 0.8$  shown as green line in Figure 10(a). The data is plotted as the function of arc length  $\xi$ , with  $\xi = 0$  corresponding to the location at the wall. The legend for the CO equation terms (b) is similar to that in Figure 11.

a zero contribution here. Closer to the wall,  $x < 0.5$  mm and  $y > 2$  mm, the source term and the flame-normal diffusion are gradually vanishing and, instead, the two tangential transport terms yield their peak locations in that area.

To display these trends in a more quantitative way, the profiles of the mass fraction of CO and the contributions of different terms are plotted in Figures 11(a) and (c) over the line indicated in yellow in Figure 10(a). This is a flamelet path located in the adiabatic area. As already seen in Figure 10, upstream from the reaction zone ( $s \approx 0$ ), convection (blue) and diffusion (red) along the flamelet pathways are in balance. There, these two transport terms are dominating the equation, while the chemical formation (yellow) and transport terms in the tangential direction are negligible. In the next part, downstream along the flamelet paths, CO is formed by chemical reactions while the diffusion tends to decrease its concentration resulting in transport along the flamelet path towards both the preheat and the post-flame zone. Finally, in the post-flame zone the CO, transported there by convection and diffusion, is consumed by chemical reactions.

Figure 11(b) and (d) shows the profiles of the mass fraction of CO and the magnitude of the terms plotted over the purple flamelet path located close to the wall (Figure 10). The following observations can be made considering this zone where the flame quenches due to the heat loss to the wall. There, the decreasing temperatures result in a vanishing source term of CO (Figure 3b). This results in an increasing difference in the concentrations between the adjacent flamelets. The arising non-zero gradient in the direction of  $\xi$ , along the flame surface, leads to significant diffusion across the flamelet paths. In this region, the

$Q$ -term (shown in green) attains the same order of magnitude as the flame-normal diffusion. This is also verified by Figure 10(d), displaying the  $Q$ -term,  $Q_{Y_{CO}}$ . As a consequence CO is being transported towards the wall. This effect is additionally illustrated in Figure 12, where the profile for the mass fraction of CO and its transformed equation terms are plotted as the function of the arc length along the flame surface, being an isocontour of progress variable at  $\mathcal{Y} = 0.8$ . The figure also depicts the enthalpy,  $h$ , and its gradient in  $\xi$ . As can be observed, the mass fraction of CO remains nearly constant in the adiabatic part of this flame surface. In this part also the terms of its transport equation in flame adaptive coordinates attain an approximately constant value. On the other hand, in the region of  $\xi$  closer to the wall, located at  $\xi = 0$ , the enthalpy gradient increases along with the contribution of the  $Q$ -term (green).

So far, the analysis is presented purely for CO, yet a similar analysis has been performed for other species, e.g. hydrogen. The observed trends are analogous to those described above for CO and the results are omitted for brevity.

An important remark should be given to conclude the observations obtained with the presented analysis of the CO governing equation. In the adiabatic part of the flame, the CO evolution qualitatively agrees with that expected in a premixed flamelet. On the other hand, the  $Q$ -term of CO attains a significant magnitude in the near-wall region. In the standard FGM approach, these terms are neglected. This again explains the limitations of the standard FGM observed in Section 3. Theoretically, in order to improve the accuracy, the FGM method can be extended by including the cross-flamelet transport terms during the generation of the flamelet data. Applying the cross-flamelet diffusion directly during the computation of the steady flamelets may, on the other hand, have a drawback of resulting in a very high numerical complexity as the solutions of all flamelets become coupled. In order to include these transport effects while retaining the ease of the application of the FGM method, a more suitable type of flamelets is utilised as described in the next section.

## 5. Manifolds based on quenching flamelets

To address the issues concluded in Sections 3 and 4, this section introduces an innovative method to extend the FGM to account for flame phenomena occurring in the presence of FWI. In Section 5.1, the generation of a 2D manifold in composition space adopting the HOQ configuration as flamelet type is presented. In this way, the enthalpy gradient is accounted for during the manifold generation. This idea is extended further in Section 5.2 by combining multiple HOQ-like simulations, each with a different rate of quenching, into a 3D manifold. The variation of the value of the enthalpy gradient at the wall is thus included in the manifold (as an extra parameter). These methods are further referred to as 2D and 3D quenching flamelet-generated manifolds in composition space ‘QFM’. In Section 5.3, the improvement in accuracy is investigated by comparing the results of the reduced chemistry SWQ modelling applying the QFMs.

### 5.1. Head on quenching flamelets for manifold generation

In analogy with [11,12], in this work an HOQ flame configuration is adopted for manifold generation as a representative flamelet type. The scalar diffusion due to the enthalpy gradient is included in an HOQ configuration. Furthermore, its solution can be found at low

computational costs using a 1D flame solver, nevertheless it incorporates a fully realistic process of FWI.

A general description of the HOQ flame configuration is given in Section 1. In this work, the HOQ flamelets are computed using the 1D laminar flame solver of Eindhoven University of Technology, **CHEM1D** [26]. The computation is performed solving the following set of equations:

$$\frac{\partial \rho}{\partial t} + \frac{\partial \rho u}{\partial x} = 0, \quad (7a)$$

$$\frac{\partial \rho Y_i}{\partial t} + \frac{\partial \rho u Y_i}{\partial x} - \frac{\partial}{\partial x} \left( \frac{\lambda}{c_p} \frac{\partial Y_i}{\partial x} \right) = \omega_i, \quad i = 1, \dots, N_s - 1, \quad (7b)$$

$$\frac{\partial \rho h}{\partial t} + \frac{\partial \rho u h}{\partial x} - \frac{\partial}{\partial x} \left( \frac{\lambda}{c_p} \frac{\partial h}{\partial x} \right) = 0, \quad (7c)$$

being respectively the equations for continuity, species transport and enthalpy for  $Le_i = 1$ . The initial condition of the time-dependent HOQ simulation corresponds to an adiabatic freely propagating premixed flame with an unburnt mixture temperature of  $T_u = 300$  K. This flame is computed separately in the pre-processing step and applied as an initial profile of the HOQ simulation. This adiabatic flame has a non-zero inlet velocity. In an HOQ simulation, a coordinate transformation is performed to a stationary frame of reference: the inlet velocity at  $x = 0$  is made zero and the velocity in the domain is corrected accordingly. In the new reference frame, an impermeable wall is located at  $x = 0$ , and the flame starts to move in the direction of the unburnt mixture and the wall. This wall is assumed to be isothermal with a temperature given by  $T_{\text{wall}} = 300$  K.

Profiles of several thermochemical quantities are shown in Figure 13 at various stages of the HOQ simulation. As the simulation time advances, the flame propagates towards the wall consuming the mixture of unburnt gas that remains between the wall and the flame zone. Upon reaching the wall, the flame starts to lose heat and eventually quenches. After a sufficiently long time the domain is filled with a mixture at chemical equilibrium at a temperature of 300 K.

After the HOQ flamelet is computed, its solution being a function of  $x$  and  $t$  can be stored in a two-dimensional manifold (2D QFM) as the function of the control variables: enthalpy,  $h$ , and progress variable,  $\mathcal{Y}$ . Figure 14(a) shows the HOQ solutions in control variable space, where each line represents one time instance. In Figure 14(b), a plot of the source term of the reaction progress variable is shown as the function of the control variables of the obtained 2D QFM. The numerical settings for the manifold tabulation and simulation setup, including the definition of the reaction progress variable, are unchanged compared to those utilised for the standard FGM (see Section 3.1). In the particular implementation strategy adopted in this work, one additional step is required during manifold generation. It involves regridding the curves of the time instances of the HOQ solution (depicted in Figure 14a) to constant enthalpy levels, which is done by linear interpolation. Subsequently, the 2D QFM can be interpolated on a curvilinear table mesh, which is schematically displayed in Figure 14(c).

Figure 15 shows with a blue dashed curve the enthalpy gradient normal to the wall boundary found in the HOQ simulation. For comparison the figure includes the curve obtained in the SWQ DC simulation from Section 2, that is shown with a solid blue curve (the remaining curves can be ignored for now). In order to make a direct comparison between the steady SWQ simulation in two spatial dimensions and the transient HOQ

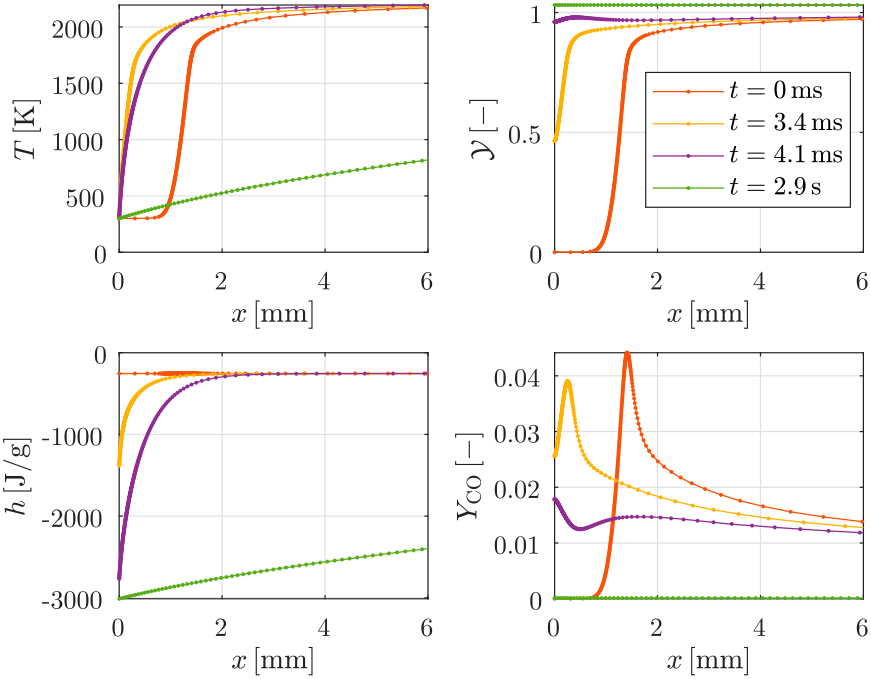


Figure 13. Thermochemical quantities at various stages of the HOQ simulation. The depicted variables are temperature  $T$ , reaction progress variable  $\mathcal{Y}$ , enthalpy  $h$  and the mass fraction of CO,  $Y_{\text{CO}}$ .

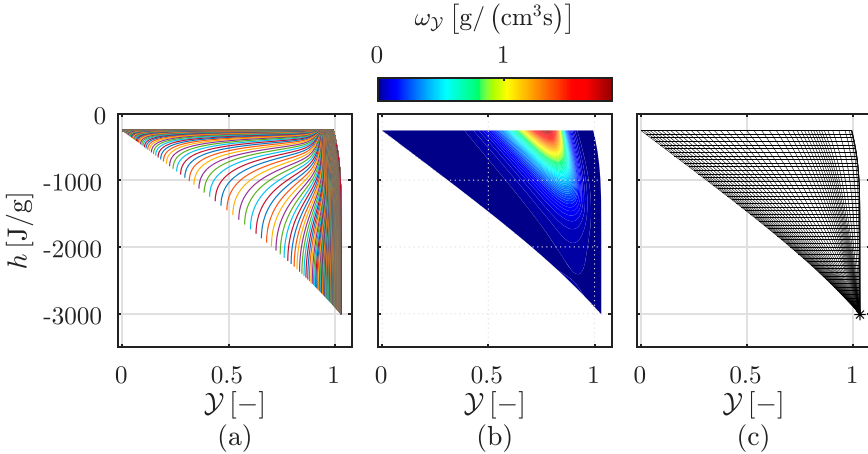


Figure 14. (a) Time instances of the HOQ simulation, (b) the source term of the progress variable and (c) the 2D QFM tabulation grid shown in the space of the FGM control variables.

results in one spatial dimension, the profiles are given as the function of enthalpy,  $h$ . Note, that both the positive  $y$  direction over the wall in the DC SWQ simulation and the positive direction of time in the HOQ case correspond to decreasing enthalpy, which is from right to left in the figure. The depicted quantity is an important parameter as it indicates

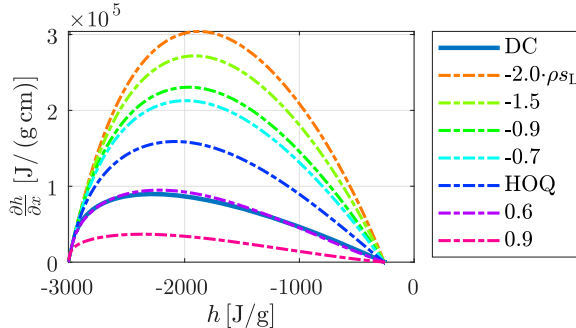


Figure 15. Normal component of the enthalpy gradient at the wall shown as the function of enthalpy for the detailed chemistry SWQ simulation, the HOQ simulation and a series of HOQ simulations with varied rate of heat loss. The values given in the legend correspond to the initial boundary mass flow rate scaled with the laminar mass burning rate, which is zero for the case of an impermeable wall in the conventional HOQ simulation.

the rate of instantaneous heat flux through the wall. As can be observed, the rate of heat loss obtained in the SWQ is two times lower than that in the HOQ. This is in agreement with the results of [12] and indicates that, even though species diffusion in direction of the enthalpy gradient is included in an HOQ configuration, its rate might be overpredicted.

### 5.2. 3D QFM: including a varying rate of cooling

In the section above, the adoption of the HOQ flamelet was discussed. It has been shown that this flamelet configuration permits, at least qualitatively, the inclusion of realistic FWI effects in the manifold composition. In counterpart to the standard constant-enthalpy flamelets, an HOQ flamelet does take into account scalar diffusion effects in the presence of enthalpy gradients. However, the *a priori* estimation of the enthalpy gradients at the wall and thus the accompanied scalar dissipation rates  $\chi_h = \lambda/\rho c_p |\nabla h|^2$  (Figure 15) has shown that in the HOQ flamelet this rate is quantitatively different compared to that in the SWQ. This rate of heat loss may have an influence on the thermochemical composition in the quenching zone.

The rate of heat loss is usually not known at the moment of generation of the manifold. Furthermore, in realistic 3D simulations and/or when turbulent FWI is involved, this rate varies as the function of position and time. In order for the FGM to be generally applicable for modelling of FWI configurations, we propose to increase the dimensionality of the manifold including the variation of the magnitude of the rate of heat loss as additional manifold variable. In order to do that, a series of HOQ flamelets needs to be computed varying this parameter. A straightforward method to increase or decrease the rate of heat loss is to artificially replace the wall (at  $x = 0$ ) by an isothermal inflow/outflow boundary (depending on the direction of the flow) imposing a prescribed mass flux through it. In this way, the velocity at which the flame approaches the wall can be controlled and varied. In the flamelet simulation, the value of the mass flow rate at this boundary,  $m_{in} = \rho u_{in}$ , can be used as a parameter to achieve a faster or a slower rate of cooling. The original HOQ simulation corresponds to  $m_{in} = 0$ . Setting  $m_{in} > 0$  results in the inlet velocity directed towards the flame, slowing the rate at which the flame is approaching the isothermal boundary and consequently decreasing the enthalpy gradients and the rate of heat loss as compared to the values in the reference HOQ simulation. On the other hand, when  $m_{in} < 0$  is set, the

boundary becomes an outflow and the flame is pulled towards the isothermal boundary. This leads to flame quenching with an increased heat loss rate.

From practical considerations, the mass flow rate at the boundary is prescribed to decrease in time as the boundary enthalpy is decreasing. This is required as the flame's burning speed is decreasing as it is losing heat and the flame would stabilise upon reaching a burning speed equal to the inlet velocity. Considering the initial value of the mass flow rate at the boundary,  $m_{\text{in}}|_{t=0}$ , the time-dependent boundary mass flow rate is prescribed as a function of the instantaneous boundary enthalpy as

$$m_{\text{in}}(t) = m_{\text{in}}|_{t=0} \cdot \left( \frac{h(t) - h_{\min}}{h_{\max} - h_{\min}} \right)^2, \quad (8)$$

where  $h_{\max}$  and  $h_{\min}$  are respectively the enthalpy of adiabatic reactant mixture and the enthalpy of the chemical equilibrium mixture at temperature of 300 K. Note that after the flame is quenched, the inlet mass flow is approaching zero. Therefore, in Equation 8 the expression for the normalised enthalpy is raised to the power 2 to ensure a faster decrease of the inlet mass flow rate as the function of enthalpy close to the  $h_{\min}$  limit. Figure 16 shows the instantaneous mass burning rate  $m_b$  for a series of HOQ simulations with varying  $m_{\text{in}}|_{t=0}$ . It is estimated by integrating the rate of heat release and plotted as the function of the enthalpy at the wall. The enthalpy at the wall, as well as in the entire domain, is decreasing as the function of time. This cooling is accompanied by the decreasing instantaneous mass burning rate, as can be observed in Figure 16. The rate of this decrease is different between the seven HOQ simulations and depends on the cooling rate. In order to prevent the flame from stabilising and to ensure that it continues to move towards the wall, the inlet mass flow has to be gradually decreased as time advances. This is achieved by setting the inlet mass flow rate lower than the instantaneous mass burning rate at the current enthalpy, which has to hold for all HOQ simulations. As shown in the figure, the simple quadratic relation from Equation (8) meets this condition. The boundary condition for the total flux  $\phi$  of species  $i$  at  $x = 0$  reads

$$\phi_i|_{x=0} = m_{\text{in}} Y_i|_{x=0}, \quad (9)$$

which results in a zero species diffusion flux at the boundary.

Figure 15 shows the normal gradients of enthalpy at the isothermal boundary. In addition to the values from the DC and the reference HOQ flamelet discussed earlier, the lines are given for a series of six HOQ simulations with varying  $m_{\text{in}}|_{t=0}$ . These simulations have either a negative or a positive value of the boundary mass flow, respectively yielding a higher or a lower rate of heat loss, as can be observed from Figure 15. To illustrate the effect of changing the rate of heat loss on the thermochemical composition in the entire series of flamelets, several thermochemical quantities are shown in Figure 17 conditioned on one level of the enthalpy,  $h \approx -920 \text{ J/g}$ . Each curve represents an individual flamelet simulation with the initial mass flow rate (scaled with the adiabatic burning rate) given in the legend. In addition, the values from the DC SWQ simulation are plotted over the enthalpy isocontour with the same level, shown by the solid line and the values found in the corresponding steady burner-stabilised flamelet (with  $h \approx -920 \text{ J/g}$ ) are given in dashed black line. The variables are plotted as the function of monotonically increasing progress variable  $\mathcal{Y}_1$ , which is not similar to that used previously for the 2D manifolds. It

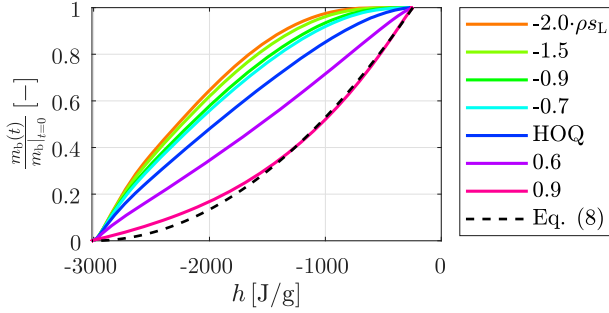


Figure 16. Scaled mass flow rate prescribed by Equation (8) and instantaneous mass burning rate of a series of HOQ simulations with varying  $m_{in}|_{t=0}$  plotted as the function of enthalpy at the wall. The values given in the legend correspond to the initial boundary mass flow rate scaled with the laminar mass burning rate, which is zero for the case of an impermeable wall in the conventional HOQ simulation.

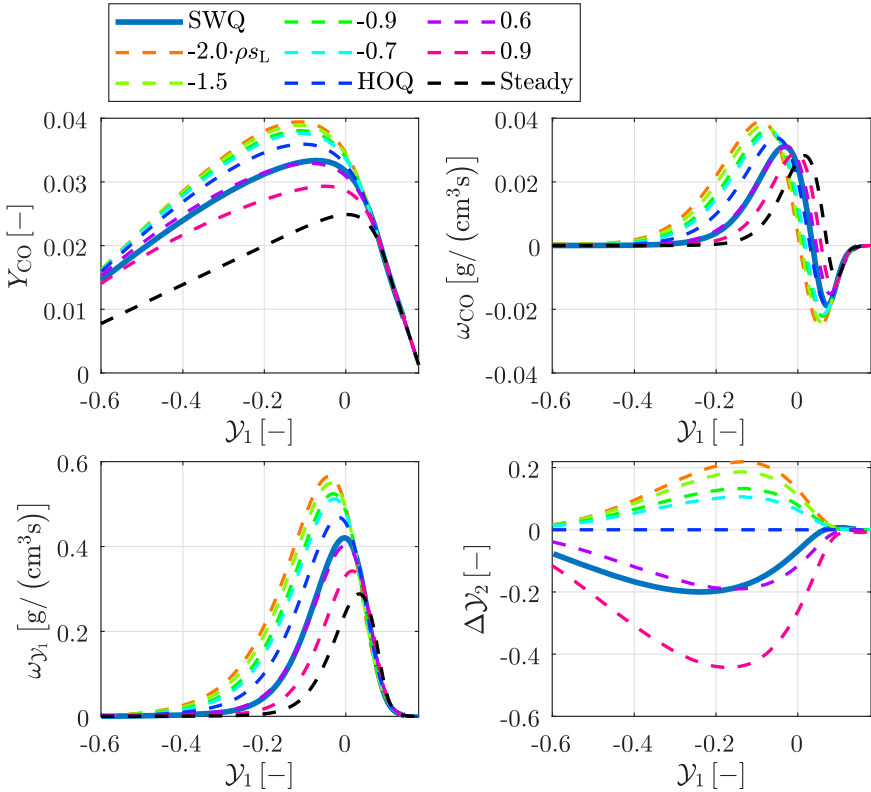


Figure 17. Mass fraction and chemical source term of CO, the source term of primary reactive control variable  $\mathcal{Y}_1$  and the surplus of the secondary reactive control variable  $\mathcal{Y}_2$  in the series of the HOQ simulations and the detailed chemistry SWQ simulation, conditioned on one level of the enthalpy,  $h \approx -920 \text{ J/g}$ . The data from a steady burner-stabilised flamelet with the same enthalpy is included in black. The variables are displayed as the function of the primary reactive control variable  $\mathcal{Y}_1$  and the values given in the legend correspond to the initial boundary mass flow rate scaled with the laminar mass burning rate, which is zero for the case of an impermeable wall in the conventional HOQ simulation.

is defined as a linear combination of species mass fractions:

$$\mathcal{Y}_j = \sum_{i=1}^{N_s} \alpha_{i,j} Y_i, \quad j = 1, \dots, N_r, \quad (10)$$

with  $j = 1$  and  $\alpha_{i,1}$  listed in Table 1. From the CO mass fraction plot in the figure it can be observed that the profiles indeed differ between the HOQ flamelets with different rates of cooling. The highest CO concentration is seen for the flamelet computed with the highest rate of cooling, corresponding to the initial mass flow rate at the boundary directed out of the domain (outflow) and being twice as large as the adiabatic mass burning rate. Furthermore, the CO mass fraction decreases with decreasing quenching rate. Finally, the lowest concentrations at this enthalpy level are observed in the profile of the steady burner stabilised flamelet. For the reaction source term of CO,  $\omega_{\text{CO}}$ , the magnitude is also decreasing with the quenching rate. In addition, the locations of its maximum and minimum values shift towards larger values of  $\mathcal{Y}_1$  with increasing quenching rate. Similar observations can be made for the source term of  $\mathcal{Y}_1$ ,  $\omega_{\mathcal{Y}_1}$ . At this enthalpy level, the DC curve is found between the reference HOQ flamelet and the flamelets with an initial mass inflow rate of 0.6 and 0.9 times the adiabatic mass burning rate. Similar behaviour was observed for other enthalpy levels. The total range of the varying heat transfer rate in the flamelet database should be chosen wide enough in order to cover its range in the final application. The range can straightforwardly be extended by computing additional HOQ flamelets with inlet mass flow rates with larger negative values than the current minimum of  $-2.0\rho s_L$ , these would yield even higher rates of heat loss compared to the current maximum.

The computed HOQ flamelets with varying rate of quenching are combined into a 3D QFM as the function of three control variables: enthalpy,  $h$ , primary reactive control variable,  $\mathcal{Y}_1$ , and the secondary reactive control variable,  $\mathcal{Y}_2$ . Where the primary one,  $\mathcal{Y}_1$ , is the reaction progress variable. The chemically reactive control variables are defined as linear combinations of species mass fractions by Equation (10), with linear coefficients respectively given by  $\alpha_{i,1}$  and  $\alpha_{i,2}$  in Table 1. The utilised tabulation procedure can be summarised as follows. First a 2D manifold is generated from each of the HOQ flamelets separately, as described in Section 5.1, and then these are combined into a 3D manifold. This work utilises a table structure facilitating a straightforward lookup. Therefore, for a single HOQ flamelet, conditioned at constant enthalpy, the progress variable  $\mathcal{Y}_1$  needs to be monotonic as the function of time. Further, the control variables should be chosen in such a way that, for given  $h$  and  $\mathcal{Y}_1$  within the manifold,  $\mathcal{Y}_2$  is a monotonic function of  $m_{\text{in}}|_{t=0}$ , the parameter of the third manifold dimension. Current definitions of the two reactive control variables have been chosen by an automated optimisation procedure<sup>2</sup> to satisfy this requirement. This is illustrated in the  $\Delta\mathcal{Y}_2$  plot in Figure 17. The depicted quantity is the difference between the local  $\mathcal{Y}_2$  value and its value corresponding to the same enthalpy and  $\mathcal{Y}_1$  in the reference HOQ flamelet simulation. As can be observed in the figure, the curves of the secondary chemically reactive control variable are, as desired, monotonically increasing following the increasing rate of heat loss between the simulations. The exact choice of the control variables is not essential as long as it results in a unique parametrisation of the manifold. The 3D manifold is stored in a table with grid size in terms of  $h \times \mathcal{Y}_1 \times \mathcal{Y}_2$  given by  $609 \times 472 \times 7$ . The grid of the  $\mathcal{Y}_2$  table dimension is non-equidistant. Therefore, a binary search method is used during lookup. Table 2 summarises the key idea of the 3D QFM method, by listing the relation between various physical effects, flamelet data parameters and the manifold control variables. The innovative aspect of the 3D QFM is to

**Table 1.** Weights of chemical species in the definitions of the reactive control variables.  $\alpha_{i,1}$  are the linear coefficients in the definition of  $\mathcal{Y}_1$ ;  $\alpha_{i,2}$  are the coefficients in the definition of  $\mathcal{Y}_2$ .  $\alpha_{i,j} = 0$  for all species  $i$  not listed in the table.

Species $i$	H <sub>2</sub>	O <sub>2</sub>	H <sub>2</sub> O	CH <sub>4</sub>	CO	CO <sub>2</sub>
$\alpha_{i,1}$	0.277	-3.881	0.050	-0.025	0	1.184
$\alpha_{i,2}$	834.7	-224.0	-30.7	80.1	-10.6	-23.7

Table 2. Relation between various physical effects, flamelet data parameters and the manifold control variables in the 3D QFM.

Physical effect	Flamelet data parameter	Parametrised by control variable
Adiabatic flame	Spatial 1D coordinate of the flamelet $Y_i = f(x)$	First reactive control variable, $\mathcal{Y}_1$ . 1D FGM, $Y_i = f(\mathcal{Y}_1)$
Heat loss	Time of the HOQ flamelet solution $Y_i = f(x, t)$	Enthalpy, $h$ . 2D QFM, $Y_i = f(\mathcal{Y}_1, h)$
Variable rate of the heat loss	Initial mass flow rate of the series of HOQ flamelets $m_{\text{in}} _{t=0}$ , $Y_i = f(x, t, m_{\text{in}} _{t=0})$	Secondary reactive control variable, $\mathcal{Y}_2$ . 3D QFM, $Y_i = f(\mathcal{Y}_1, h, \mathcal{Y}_2)$

include the cooling rate as a variable parameter of the system. Note that the cooling rate does not need to be computed explicitly, instead its parametrisation is allowed by including the secondary reactive control variable, as indicated in the table.

When the 3D QFM is applied in the SWQ simulation, a transport equation for enthalpy, Equation (1d), and transport equations for both chemically reactive control variables, given by

$$\nabla \cdot (\rho \mathbf{u} \mathcal{Y}_j) - \nabla \cdot \left( \frac{\lambda}{c_p} \nabla \mathcal{Y}_j \right) = \omega_{\mathcal{Y}_j}, \quad j = 1, \dots, N_r (= 2), \quad (11)$$

with  $N_r$  being the number of reactive control variables in the manifold, are solved in addition to the Navier–Stokes equations (Equations 1a and 1b). During runtime, the dependent thermochemical quantities are looked up in the manifold by means of tri-linear interpolation as the function of  $h$ ,  $\mathcal{Y}_1$  and  $\mathcal{Y}_2$ .

### 5.3. QFM simulation results

In this section, the results of the SWQ reduced modelling obtained with the 2D QFM generated from the reference HOQ flamelet and the 3D QFM extended with the variation of the rate of wall heat loss as additional parameter are presented and discussed. Figure 18 depicts the heat flux to the wall obtained with the presented models. As can be observed, below  $y = 2.5$  mm all the three models are in agreement with DC. Further downstream, the 2D FGM underestimates the peak of the heat loss, while the 2D QFM shows an over-estimation. The results obtained with the 3D QFM yield a very accurate prediction of the heat loss over the entire height of the wall. Figure 19 shows the contour plots for progress variables and enthalpy found with the QFMs. Note that the reaction progress variables for the two manifolds are based on dissimilar definitions. For the 2D manifold  $\mathcal{Y}$  is displayed, while for the 3D QFM  $\mathcal{Y}_1$  is shown. As can be seen, the 2D manifold yields a good qualitative agreement for the progress variable and enthalpy. In counterpart to the standard

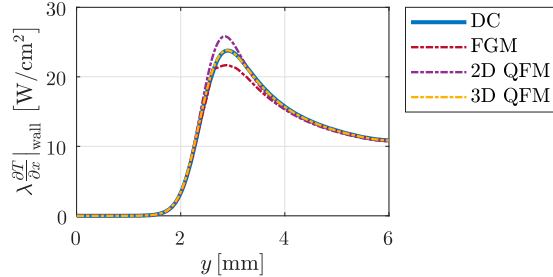


Figure 18. Simulation results for the heat flux to the wall as function of  $y$  (at  $x = 0$  mm).

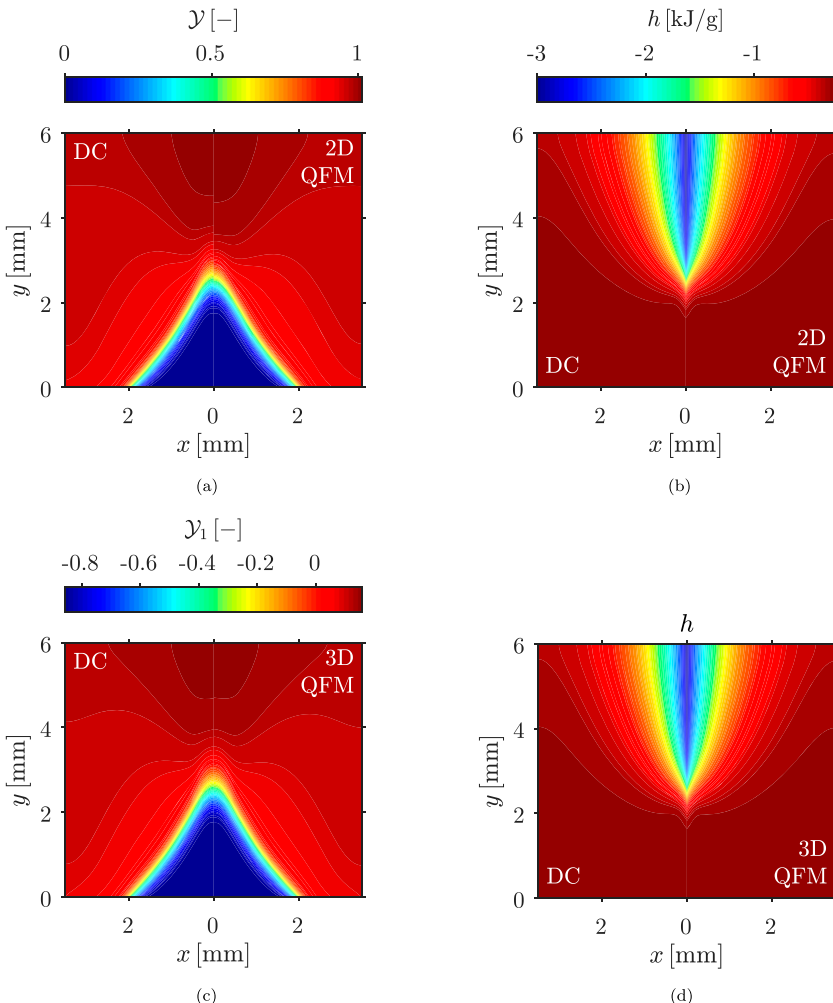


Figure 19. 2D and 3D QFM simulation results for the two control variables: reaction progress variable and enthalpy  $h$ . The two manifolds utilise different definitions of the reaction progress variable, those are denoted by  $\mathcal{Y}$  in case of 2D QFM and by  $\mathcal{Y}_1$  in case of the 3D QFM. The DC results are shown as reference at the left of each plot.

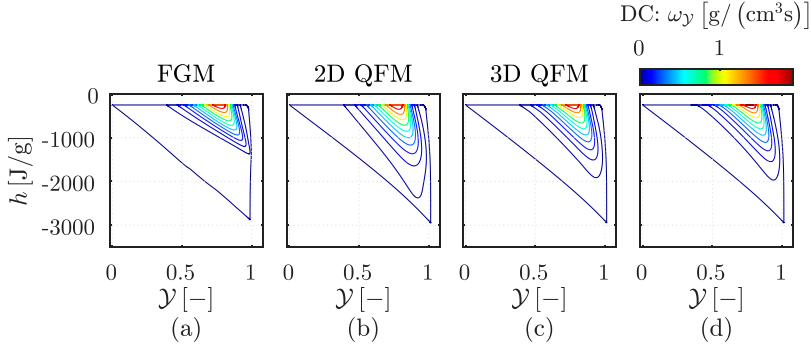


Figure 20. Source term of the reaction progress variable  $\omega_Y$  found with the three reduced models shown in the space of control variables,  $\mathcal{Y}$  and  $h$ . For comparison, detailed chemistry results are shown in the right plot.

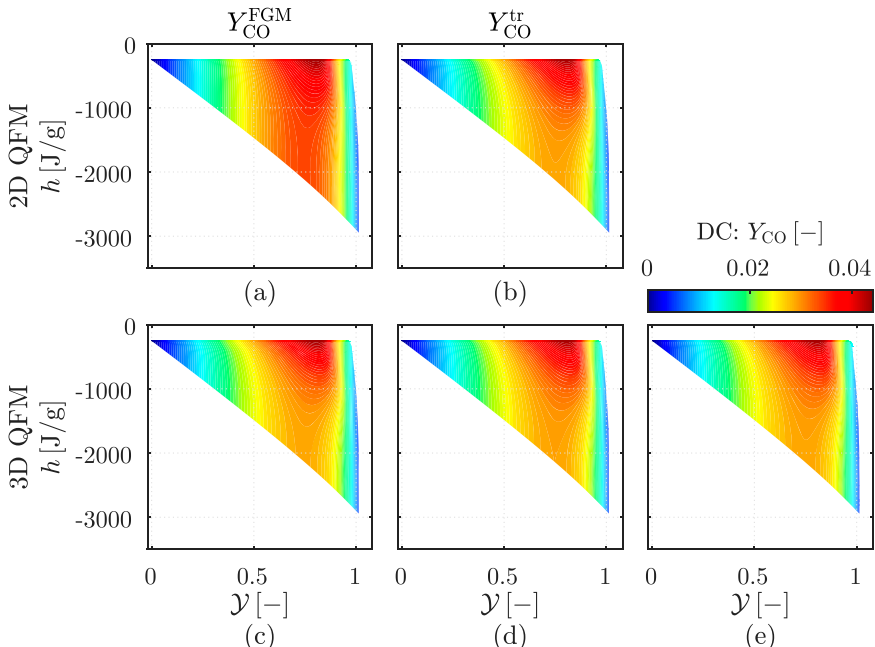


Figure 21. Mass fraction of CO for 2D QFM (upper row) and 3D QFM (lower row) shown in the space of control variables,  $\mathcal{Y}$  and  $h$ . Left column: Value obtained by direct lookup. Center column: QFM simulation results for CO obtained by solving an additional transport equation for  $Y_{CO}^{tr}$ . Right column: Detailed chemistry results for CO.

FGM (see Section 3.3) it accurately predicts the shape of the progress variable in the non-adiabatic post-flame area. Though, quantitatively, it is overpredicting the progress variable in the quenching zone, as the location where the flame touches the wall is shifted to lower  $y$  coordinates. Away from the wall, a good agreement for the control variables is obtained with the 2D QFM. The 3D QFM method, on the other hand, shows a very good quantitative agreement for these variables also in the near-wall region: the locations of the isocontours of its reaction progress variable  $\mathcal{Y}_1$  and enthalpy correctly coincide with those predicted

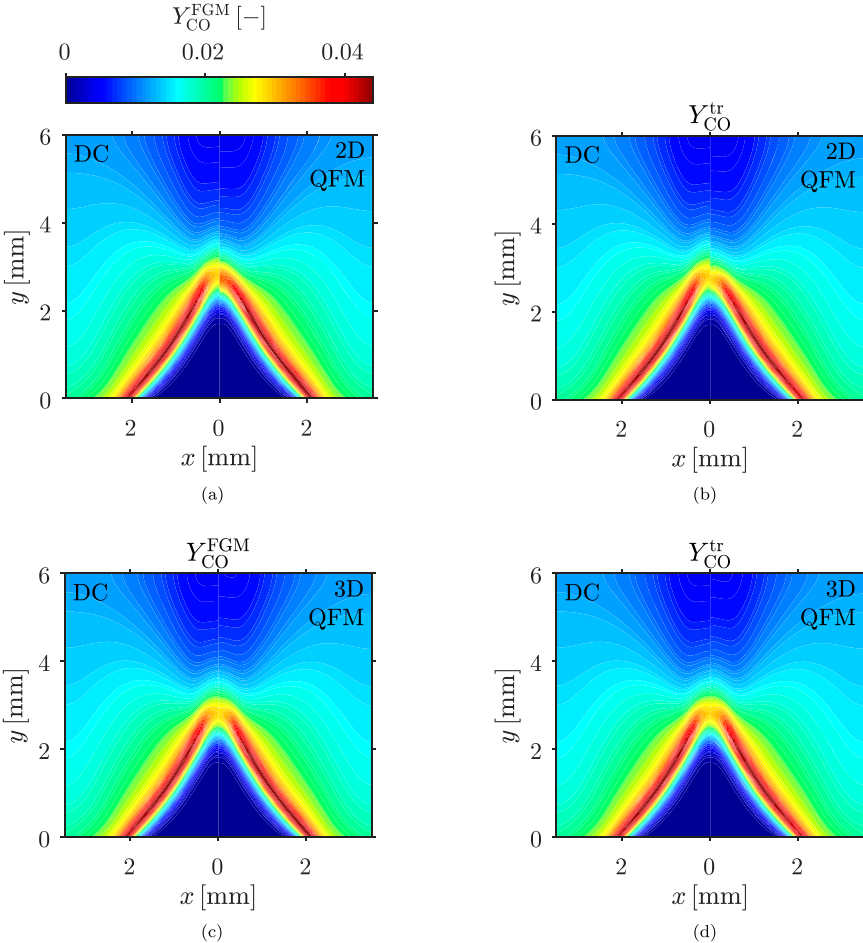


Figure 22. 2D and 3D QFM simulation results for the mass fraction of CO found by direct lookup ( $Y_{\text{CO}}^{\text{FGM}}$ ) and a transport equation including a two-way coupling for the source term ( $Y_{\text{CO}}^{\text{tr}}$ ).

by the DC model. Also, globally in the entire domain, 3D QFM yields high accuracy for the control variables. To explain the difference between the progress variable results of the reduced models, progress variable source term  $\omega_y$  is shown for the detailed and the reduced models in Figure 20 parametrised in terms of the control variables composition. As can be observed, the 3D QFM shows the best agreement with the detailed chemistry. On the other hand, the standard FGM underpredicts and the 2D QFM overpredicts the progress variable source term, which translates to inaccuracies for progress variable found with these reduced models.

Figures 21 and 22 demonstrate the CO results found with the 2D and the 3D QFMs, shown respectively in the space of the control variables ( $\mathcal{Y}, h$ ) and in physical space ( $x, y$ ). The CO values found by direct lookup and by solving a transport equation as explained in Section 3.2 are displayed along the DC results, which are used as reference. For the 2D QFM, the direct lookup results show a higher magnitude of the mass fraction in the region where the flame is quenching along the wall, which becomes apparent from

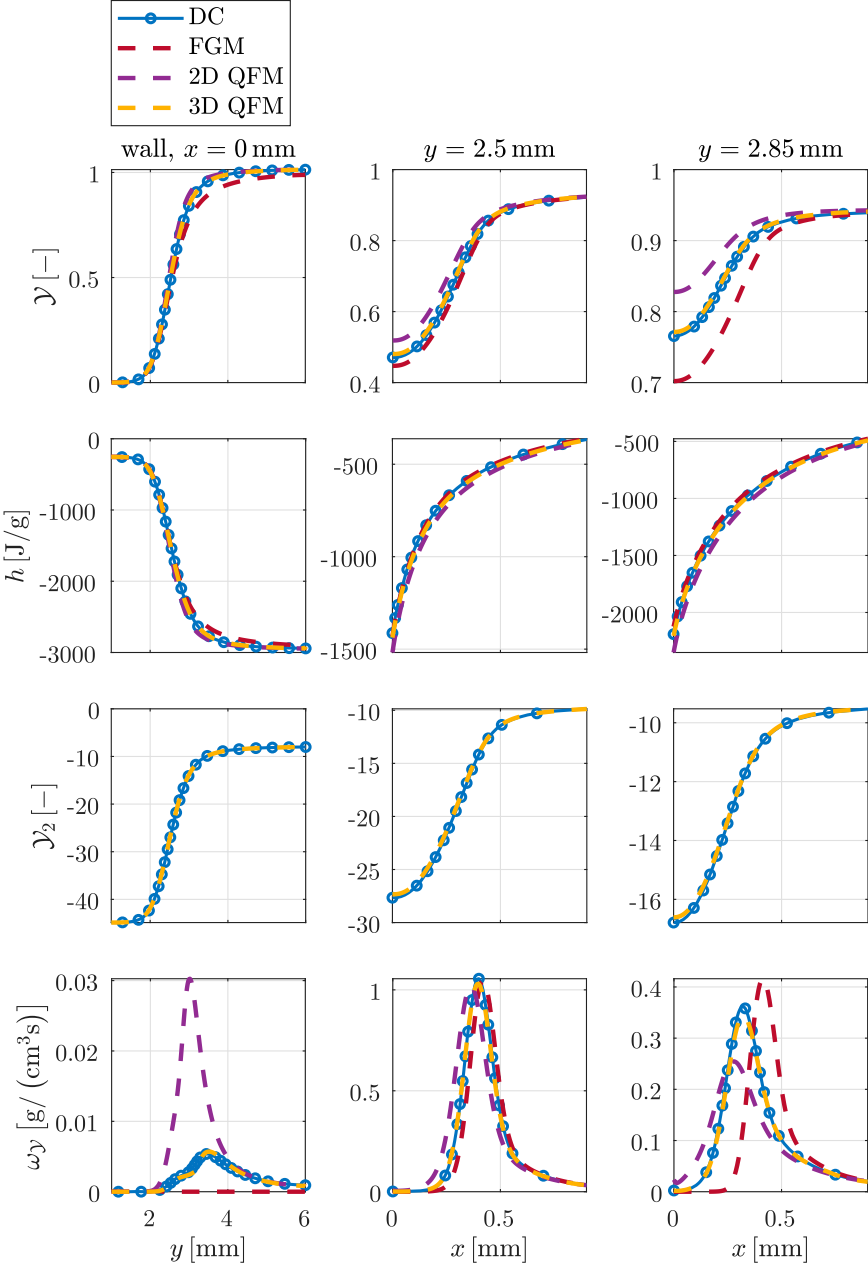


Figure 23. Profiles of various thermochemical variables, top to bottom: progress variable  $\mathcal{Y}$ , enthalpy  $h$ , secondary reactive control variable of the 3D QFM ( $\mathcal{Y}_2$ ) and the source term of the progress variable  $\omega_{\mathcal{Y}}$ , at the left as the function of  $y$  over the wall ( $x = 0 \text{ mm}$ ), in the middle and at the right as the function of  $x$  at respectively  $y = 2.5 \text{ mm}$  and  $2.85 \text{ mm}$ .

the contours plotted as function of the control variables in Figure 21(a). The transported CO can be observed to yield a much better magnitude (Figure 21b). However, looking at the results displayed in physical space in Figures 22(a) and (b), both CO models applied in

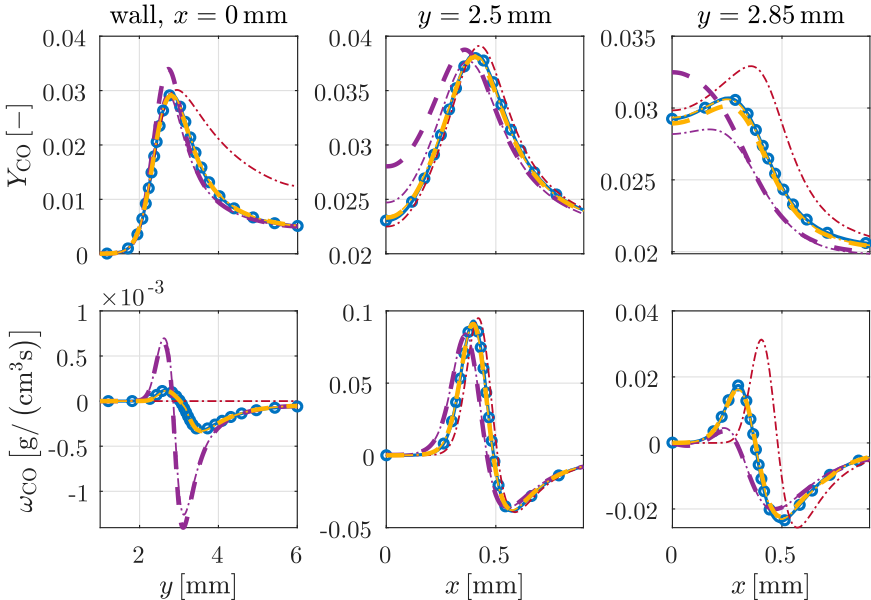


Figure 24. Profiles of CO mass fraction and source term plotted as the function of  $y$  over the wall ( $x = 0 \text{ mm}$ ) and as the function of  $x$  over the wall-normal lines at  $y = 2.5 \text{ mm}$  and  $y = 2.85 \text{ mm}$ . The two CO modelling methods are shown by different line styles as indicated in the legend of Figure 9. The legend for the line colours depicting different chemistry models (DC, standard FGM, 2D QFM and 3D QFM) is given in Figure 23.

the context of the 2D QFM yield the peak values located at a slightly lower  $y$ -coordinate along the wall. In analogy with the standard FGM results presented in Section 3.3, this is attributed to the inaccuracy of the progress variable, which is overpredicted in the case of the 2D QFM. In counterpart, the 3D QFM correctly predicts the location and the magnitude of the CO mass fraction. Applying a transport equation for CO in the context of the 3D QFM only slightly improves the accuracy compared to direct lookup. The fact that the transported CO results are not much different from those obtained by direct lookup, indicates that the transport-related perturbations of CO from the local values in the 3D manifold are small.

The results of the simulations can be observed in more detail in Figures 23 and 24, showing the profiles for several quantities plotted, respectively, over the wall and the two wall-normal lines shown in Figure 5(a). The trend observed for the 2D QFM is reversed to that seen previously for the standard FGM: the progress variable growth rate is overpredicted. This can be explained by looking back at Figure 15, which shows that the rate of heat loss to the wall in the reference HOQ flamelet is twice as high compared to that in the detailed SWQ simulation. The discrepancies observed for the remaining variables are also caused by the underlying flamelet being based on an overestimated magnitude of the rate of scalar diffusion due to the enthalpy gradient. The inaccuracies are further magnified by the incorrect spatial distribution of the control variables. The 3D QFM on the other hand accounts for a range of possible heat loss rates, yielding accurate results for both the control variables and the dependent thermochemical quantities.

The following can be stated to summarise the discussion of the results obtained utilising the three reduced chemistry methods. It can be concluded that for the standard FGM and

the 2D QFM the major discrepancies compared with the detailed chemistry arise due to inaccurate predictions of the control variables, especially the reaction progress variable  $\mathcal{Y}$ . The inaccuracies in the prediction of the progress variable source term are a direct result of the species composition in the manifold not being accurate, because the reaction rates stored in the manifold are dependent on the underlying species composition. Nearly all other chemical species, when looked up directly in these 2D manifolds, yield prediction inaccuracies similar to that seen for CO. The scalar dissipation arising in the presence of a high enthalpy gradient in the near-wall region plays an important role also for the remaining species. In the detailed chemistry simulation, the components of the mixture attain values different to those in the standard FGM and the 2D QFM. On the other hand, for the 3D QFM it is interesting to note that the mass fraction of CO in the manifold (direct lookup) and the transported CO mass fraction are almost identical, indicating that the CO values in the manifold meet the physics experienced in the SWQ simulation. For chemical species other than CO, no transport equations have been solved in the 3D QFM simulation. However, it has been verified that their values are being predicted with a high accuracy simply using direct lookup, resulting in correct values for the control variables and their source terms. For the profiles of several other species, the reader is referred to the figures in the supplementary materials.

## 6. Conclusion

In this paper, an innovative method has been proposed which has the objective to extend FGM in order to account for the effects of FWI on the formation of pollutants. The developed model has been validated utilising a two-dimensional simulation of SWQ of a premixed methane–air flame.

The analysis of the detailed chemistry simulation has revealed a strong dependence of the CO concentrations on the gradients of enthalpy in the near-wall region. It has been attributed to the scalar diffusion due to the enthalpy gradient, which had not yet been included in standard FGM modelling utilising steady flamelets with constant enthalpy.

The solution proposed here involves adopting the 1D HOQ flame simulations for the generation of the manifolds, referred to as quenching flamelet manifolds QFM. In this way, the effects of scalar dissipation in the direction of enthalpy can be included in the manifold. In order to account for the variation of the enthalpy gradients, a method utilising a 3D QFM has been developed, incorporating this variation as an additional degree of freedom.

It has been demonstrated that the tabulated chemistry CO accuracy in the SWQ simulation improves applying the 2D QFM and that a very high accuracy is obtained utilising the 3D QFM method. Solving an additional transport equation for CO mass fraction in the context of the FGM model generally improves the results compared to the conventional method looking up the CO directly from the manifold. However, the quality of the representation of the thermochemical composition has a large influence on the (transported) CO accuracy. It can be concluded that the 3D QFM method, including an additional dimension, yields a very accurate representation of the thermochemical composition. In general, without the need for any ad-hoc estimations during the manifold generation, the 3D QFM results in a better prediction of the major properties of the flame involving FWI. This directly translates into improved CO accuracy.

There still remains a potential to further improve this model and its validation. In this work, the 3D QFM has been applied to a laminar flame with a relatively low rate of heat loss at the wall. In future work, this method can be challenged to simulate a configuration with higher enthalpy gradients in the near-wall region. The heat transfer rates can be varied for instance by applying different inlet velocities or unsteady phenomena. Although the flamelet data suitable for FWI with higher enthalpy gradients was included in the current manifold, these conditions were not encountered in the present test case. Several other physical effects can still be included in the modelling approach, such as preferential diffusion and FWI in turbulent flames.

### Disclosure statement

No potential conflict of interest was reported by the authors.

### Supplementary Material

Supplemental data for this article can be accessed at <https://doi.org/10.1080/13647830.2019.1658901>.

### Notes

1. ANSYS® Fluent, Release 18.2
2. The optimisation is not done simultaneously for both reactive control variables. On the contrary, first the coefficients of  $\mathcal{Y}_1$  are obtained and, using these, another separate optimisation is performed to obtain the coefficients of  $\mathcal{Y}_2$ .

### ORCID

Denis V. Efimov  <http://orcid.org/0000-0002-2875-2146>

Philip de Goey  <http://orcid.org/0000-0001-6625-3113>

Jeroen A. van Oijen  <http://orcid.org/0000-0002-4283-2898>

### References

- [1] T. Poinsot and D. Veynante, *Theoretical and numerical combustion*, 2nd ed., Philadelphia, 2005.
- [2] Zbigniew J. Sroka, *Some aspects of thermal load and operating indexes after downsizing for internal combustion engine*, J. Therm. Anal. Calorim. 110(1) (2012), pp. 51–58.
- [3] U. Stopper, W. Meier, R. Sadanandan, M. Stöhr, M. Aigner, and G. Bulat, *Experimental study of industrial gas turbine flames including quantification of pressure influence on flow field, fuel/air premixing and flame shape*, Combust. Flame. 160(10) (2013), pp. 2103–2118.
- [4] Y. Huang and V. Yang, *Bifurcation of flame structure in a lean-premixed swirl-stabilized combustor: Transition from stable to unstable flame*, Combust. Flame 136(3) (2004), pp. 383–389.
- [5] O. Ezekoye, R. Greif, and R.F. Sawyer, *Increased surface temperature effects on wall heat transfer during unsteady flame quenching*, Symp. (Int.) Combustion 24(1) (1992), pp. 1465–1472.
- [6] P. Popp and M. Baum, *Analysis of wall heat fluxes, reaction mechanisms, and unburnt hydrocarbons during the head-on quenching of a laminar methane flame*, Combust. Flame 108(3) (1997), pp. 327–348.
- [7] J.H. Lu, O. Ezekoye, R. Greif, and R.F. Sawyer, *Unsteady heat transfer during side wall quenching of a laminar flame*, Symp. (Int.) Combust. 23(1) (1991), pp. 441–446.

- [8] J. Andrae, P. Björnbom, L. Edsberg, and L.E. Eriksson, *A numerical study of side wall quenching with propane/air flames*, Proc. Combust. Inst. 29(1) (2002), pp. 789–795.
- [9] P. Zhao, L. Wang, and N. Chakraborty, *Analysis of the flame-wall interaction in premixed turbulent combustion*, J. Fluid Mech. 848 (2018), pp. 193–218.
- [10] S. Ganter, A. Heinrich, T. Meier, G. Kuenne, C. Jainski, M.C. Rißmann, A. Dreizler, and J. Janicka, *Numerical analysis of laminar methane air side-wall-quenching*, Combust. Flame 186 (2017), pp. 299–310.
- [11] G. Steinhilber, V. Bykov, and U. Maas, *REDIM reduced modeling of flame-wall interactions: Quenching of a premixed methane/air flame at a cold inert wall*, Proc. Combust. Inst. 36(1) (2017), pp. 655–661.
- [12] S. Ganter, C. Straßacker, G. Kuenne, T. Meier, A. Heinrich, U. Maas, and J. Janicka, *Laminar near-wall combustion: Analysis of tabulated chemistry simulations by means of detailed kinetics*, Int. J. Heat Fluid Flow 70 (2018), pp. 259–270.
- [13] J.A. van Oijen and L.P.H. de Goey, *Modelling of premixed laminar flames using flamelet-generated manifolds*, Combust. Sci. Technol. 161 (2000), pp. 113–137.
- [14] J.A. van Oijen, F.A. Lammers, and L.P.H. de Goey, *Modeling of complex premixed burner systems by using flamelet-generated manifolds*, Combust. Flame 127(3) (2001), pp. 2124–2134.
- [15] J.A. Van Oijen and L.P.H. De Goey, *Modelling of premixed counterflow flames using the flamelet-generated manifold method*, Combust. Theory Model. 6(3) (2002), pp. 463–478.
- [16] A. Gruber, R. Sankaran, E.R. Hawkes, and J.H. Chen, *Turbulent flame-wall interaction: A direct numerical simulation study*, J. Fluid Mech. 658 (2010), pp. 5–32.
- [17] A. Heinrich, *Large Eddy Simulation with tabulated chemistry of an experimental sidewall quenching burner*, Int. J. Heat Fluid Flow 71(march) (2018), pp. 95–110.
- [18] D.V. Efimov, P. de Goey, and J.A. van Oijen, *FGM with REDx: chemically reactive dimensionality extension*, Combust. Theory Model. 0(0) (2018), pp. 1–31.
- [19] A. Kazakov and M. Frenklach, DRM19. Available at <http://www.me.berkeley.edu/drm/>, 1994.
- [20] A. Donini, R.J.M. Bastiaans, J.A. van Oijen and L.P.H. de Goey, *Differential diffusion effects inclusion with flamelet generated manifold for the modeling of stratified premixed cooled flames*, Proc. Combust Inst. 35(1) (2015), pp. 831–837.
- [21] E. Abtahizadeh, P. de Goey and J. van Oijen, *Development of a novel flamelet-based model to include preferential diffusion effects in autoignition of CH<sub>4</sub>/H<sub>2</sub> flames*, Combust. Flame 162(11) (2015), pp. 4358–4369.
- [22] W.P. Jones and C.H. Priddin, Predictions of the flow field and local gas composition in gas turbine combustors. *Proc. Combust Inst.*, vol. 17, pp. 399–408, 1978.
- [23] A.W. Vreman, B.A. Albrecht, J.A. van Oijen, L.P.H. de Goey and R.J.M. Bastiaans, *Premixed and nonpremixed generated manifolds in large-eddy simulation of Sandia flame D and F*, Combust. Flame 153(3) (2008), pp. 394–416.
- [24] M. Ihme and H. Pitsch, *Modeling of radiation and nitric oxide formation in turbulent non-premixed flames using a flamelet/progress variable formulation*, Phys. Fluids 20 (2008), p. 055110.
- [25] J.A. van Oijen, A. Domini, R.J.M. Bastiaans, J.H.M. ten Thije Boonkamp, and L.P.H. de Goey, *State-of-the-art in premixed combustion modeling using flamelet generated manifolds*, Prog. Energy Combust. Sci. 57 (2016), pp. 30–74.
- [26] Eindhoven University of Technology. CHEM1D. Available at [www.combustion.tue.nl](http://www.combustion.tue.nl).